



**LOW FREQUENCY MATERIAL CHARACTERIZATION OF THIN
SUBSTRATES IN A COAXIAL TRANSMISSION LINE**

THESIS

Lee B. Cole, Captain, USAF

AFIT/GE/ENG/12-10

**DEPARTMENT OF THE AIR FORCE
AIR UNIVERSITY**

AIR FORCE INSTITUTE OF TECHNOLOGY

Wright-Patterson Air Force Base, Ohio

DISTRIBUTION STATEMENT A
APPROVED FOR PUBLIC RELEASE; DISTRIBUTION UNLIMITED

The views expressed in this thesis are those of the author and do not reflect the official policy or position of the United States Air Force, Department of Defense, or the United States Government. This material is declared a work of the U.S. Government and is not subject to copyright protection in the United States.

AFIT/GE/ENG/12-10

**LOW FREQUENCY MATERIAL CHARACTERIZATION OF THIN
SUBSTRATES IN A COAXIAL TRANSMISSION LINE**

THESIS

Presented to the Faculty

Department of Electrical and Computer Engineering

Graduate School of Engineering and Management

Air Force Institute of Technology

Air University

Air Education and Training Command

In Partial Fulfillment of the Requirements for the
Degree of Master of Science in Electrical Engineering

Lee B. Cole, B.S.E.E

Captain, USAF

March 2012

DISTRIBUTION STATEMENT A
APPROVED FOR PUBLIC RELEASE; DISTRIBUTION UNLIMITED

**LOW FREQUENCY MATERIAL CHARACTERIZATION OF THIN
SUBSTRATES IN A COAXIAL TRANSMISSION LINE**

Lee B. Cole, B.S.E.E

Captain, USAF

Approved:

// SIGNED //
Dr. Michael J. Havrilla (Chairman)

7 Mar 2012
Date

// SIGNED //
Dr. William P. Baker (Member)

7 Mar 2012
Date

// SIGNED //
Maj. Milo W. Hyde, Ph.D. (Member)

2 Mar 2012
Date

ABSTRACT

This research analyzes the complex permittivity and permeability of thin samples of materials with large air gaps between the material sample and outer conductor of a coaxial waveguide. Assuming axially symmetric air gaps, higher order fields are excited in the sample region which must be accounted for due to the power coupling into these higher order fields. This work builds upon previous research which analyzed the effects of smaller air gaps on the extracted material parameters of both dielectric and magnetic material samples.

This research utilizes the modal method developed in the previous research to calculate theoretical scattering parameters of the sample region as a function of permittivity, permeability, and frequency. Complex root search algorithms (either a Newton or Levenberg-Marquardt) iterate the values of permittivity and permeability until the difference between the theoretical and measured scattering parameters is minimized. The final theoretical permittivity and permeability values are determined to be the actual properties of the material sample.

Accurate results were obtained for a dielectric sample which filled only 22% of the radial distance between inner and outer conductors when considering 20 modes. It is shown that the solution appears to converge after consideration of only 10 modes.

When utilized with 20 mil samples of the magnetic material WaveX filling only 12.5% of the distance between inner and outer conductors, the modal method returned very poor results for permittivity and relatively accurate permeability results. The

WaveX samples were cut from flat sheets of material and “wrapped” around the inner conductor, likely resulting in errors which are not accounted for in the modal method development. Additionally, the material exhibited strong anisotropic tendencies which also were not accounted for in the modal method development. It appears that the higher order modes evanesce much more rapidly than in the dielectric material case, resulting in less impact to the system.

Two sources of error likely significantly degraded the effectiveness of the modal method for the thin WaveX samples. The first source is measurement error which is attributed to the discontinuities created when wrapping the material around the conductor. This likely invalidated the assumption of axial symmetry which would lead to a more complex field development. The second error source is the assumption of a simple media (i.e. linear, isotropic, and homogeneous). It was discovered by the end of this research that the WaveX is in fact highly anisotropic. This fact would lead to an entirely different field development which would greatly impact the results of the modal method.

ACKNOWLEDGMENTS

I wish to express my appreciation to my faculty advisor, Dr. Michael Havrilla, for his guidance and support throughout the course of this effort. His insistence on the understanding of the physical nature behind the problem has given me a greater insight and respect for the wonderful order present in the study of electromagnetics. I also greatly appreciate the insight and assistance of my other committee members, Dr. William Baker and Maj. Milo Hyde as they helped shepherd me through much of the experimental and computational portions of this research. Without their hands on assistance, this effort certainly would not have been possible.

Finally I wish to thank my wife and daughter for their unending love and support throughout this effort. Their patient understanding and encouragement lifted my spirits and helped me see this effort through to completion.

Lee B. Cole

TABLE OF CONTENTS

	Page
ABSTRACT.....	iv
ACKNOWLEDGEMENTS.....	vi
TABLE OF CONTENTS.....	viii
LIST OF FIGURES	ix
LIST OF TABLES	xii
LIST OF ABBREVIATIONS.....	xiii
I. INTRODUCTION.....	1
1.1 Problem Statement.....	2
1.2 Limitations	5
1.3 Scope.....	6
1.4 Thesis Organization	7
II. BACKGROUND.....	8
2.1 Transmission/Reflection (TR) Method and Coaxial Waveguides	8
2.2 The TEM Coaxial Waveguide	10
2.3 Air Gap Correction Efforts	16
2.3.1 Circuit Model Corrections.....	17
2.3.2 Modal Analysis.....	20
2.4 Numerical Root Searching.....	24
2.5 Summary	25
III. METHODOLOGY	27
3.1 Modal Method Development for a TEM Coaxial Waveguide.....	28
3.2 Low Frequency Stripline Method	41
3.3 Summary	44
IV. RESULTS.....	45
4.1 Test Setup.....	45
4.2 Modal Method Performance	49
4.2.1 Performance for a Thin Dielectric.....	49
4.2.2 Performance for WaveX.....	54
4.3 Wavenumber Calculations	59

V. CONCLUSIONS AND RECOMMENDATIONS.....	63
5.1 Future Research	64
5.1.1 Air Gap Sensitivity Analysis	64
5.1.2 Compensation for Anisotropic Materials	65
APPENDIX A Maxwell's Equations.....	66
APPENDIX B Helmholtz Wave Equations & Vector Potentials	68
APPENDIX C Fields in a Coaxial Waveguide.....	72
APPENDIX D GTRI WaveX Results.....	78
BIBLIOGRAPHY.....	80

LIST OF FIGURES

Figure		Page
1.1.	Thin material sample Coaxial Line Concept	7
2.1.	14mm Coaxial Transmission Line	11
2.2.	Coaxial line cross sections (Filled and Air Gap)	11
2.3.	Partially filled coaxial line mode structure	13
2.4.	Inner and Outer air gap diagram and dimensions for the Lumped circuit correction factor	17
2.5.	NRW performance and NIST corrected values for the 123.5 mil outer air gap unknown dielectric sample	22
2.6.	NRW performance and NIST corrected values for the 139 mil outer air gap WaveX sample	23
2.7.	10 mode correction to MagRAM with a 9 mil air gap	24
3.1.	Mode coupling in the partially filled coaxial line	28
3.2.	Low frequency stripline diagram	44
4.1.	Coaxial transmission line components.....	47
4.2.	Assembled coaxial transmission line	47
4.3.	1D root search 20 mode correction to unknown dielectric with a 123.5 mil outer air gap	51
4.4.	S_{11} and S_{21} magnitudes of a unknown dielectric with a 123.5 mil out air gap	51
4.5.	2D root search 20 mode correction to unknown dielectric with a 123.5 mil outer air gap	52
4.6.	Mode sweep of a 123.5 mil out air gap dielectric	53

4.7.	Perturbation analysis complex permittivity of a dielectric with a 123.5 mil outer air gap	53
4.8.	dB magnitude of S_{11} for a 139 mil outer air gap sample of 20 mil thick WaveX	55
4.9.	5 mode correction to WaveX with a 139 mil outer air gap using both S_{11} and S_{21}	55
4.10.	4 mode correction to WaveX with a 139 mil outer air gap using two independent S_{21} measurements	56
4.11.	Extracted complex permittivity and permeability of WaveX in a low frequency stripline	58
4.12.	Extracted complex permittivity and permeability of Plexiglass in a low frequency stripline	58

LIST OF TABLES

Table		Page
2.1.	Inner and Outer air gap diagram and dimensions for the Lumped circuit correction factor	10
4.1.	Comparison of wavenumbers in an empty coaxial line and a dielectric filled line with a 123.5 mil outer air gap	62
4.2.	Comparison of calculated wavenumbers in a WaveX filled line with a 139 mil outer air gap using the step/perturbation method and Muller's method	62

LIST OF ABBREVIATIONS

Abbreviation		Page
EMI	Electromagnetic Interference	1
EMC	Electromagnetic Compatibility	1
AFRL/RY	Air Force Research Laboratory, Sensors Directorate	2
TEM	Transverse Electromagnetic	2
TR	Transmission/Reflection	3
NWA	Network Analyzer	3
NRW	Nicolson-Ross-Weir	3
GTRI	Georgia Tech Research Institute	5
TM	Transverse Magnetic	12
TE	Transverse Electric	12
PEC	Perfect Electric Conductor	15
NIST	National Institute of Standards and Technology	17
MagRAM	Magnetic Radar Absorbing Material	22
LM	Levenberg-Marquardt	25
1D	One-Dimensional	45
2D	Two-Dimensional	45
TRL	Thru, Reflect, Line	46

LOW FREQUENCY MATERIAL CHARACTERIZATION OF THIN SUBSTRATES IN A COAXIAL TRANSMISSION LINE

I. INTRODUCTION

All materials contain certain intrinsic properties which determine their response to electromagnetic fields in the environment. In today's high technology environment, electromagnetic fields are ever present from applications ranging from personal communications to defense applications such as threat radars. This proliferation of electromagnetic energy drives the need to continue developing new materials with specific responses to these electromagnetic fields. The electromagnetic characteristics of these materials, primarily permittivity and permeability, are the core to understanding the material's response to an induced electric and magnetic field respectively.

A classic example of an application in which this knowledge is critical is the field of electromagnetic interference and compatibility (EMI/EMC). Most modern electronic devices work in close proximity to each other and therefore can be susceptible to electromagnetic interference from each other. To overcome this interference, certain materials may be incorporated into the device to act as a shield to prevent unwanted external energy from penetrating the device. EMI/EMC can prove to be a very large threat to complex systems such as aircraft due to their operating environment and onboard high power communications and navigation equipment. Today's military aircraft employ a variety of materials in their design which serve as shields to protect

vital systems such as avionics and munitions from this external electromagnetic interference. These materials are designed to absorb some of this energy, preventing it from reaching the critical systems, and lower the amount that might be scattered back into the environment.

These materials are becoming increasingly thin and flexible thanks to furthered understanding in materials science and advances in manufacturing technologies. One problem created with these more complex materials is the performance of traditional methods used to characterize the permittivity and permeability of the material. This drives the need to develop novel techniques that quickly and accurately determine these properties in a non-destructive manner.

1.1 Problem Statement

The sponsor of this research, the Air Force Research Laboratory, Sensors Directorate (AFRL/RYS), expressed interest in the electromagnetic characterization of thin materials in low frequency environments. Many techniques such as transmission lines, cavities, free-space systems and striplines currently exist to measure a material's electromagnetic properties at varying frequency ranges. Low frequency characterization carries inherent challenges, most notably the sample size required for accurate measurements at these frequencies. Many of these techniques previously mentioned require impractically large sample sizes; therefore, many traditional methods are eliminated from consideration.

One technique which shows promise and is the focus of investigation in this research is the TEM coaxial transmission line/waveguide. The design of the TEM line

allows for low frequency interrogation using relatively small sample sizes. Additionally, the coaxial line has a normal (i.e. radial) or vertically polarized electric field to samples which are wrapped around the inner or outer conductors. This allows for a strong traveling-wave field interrogation of a thin material wrapped around either conductor. Additionally, the coaxial line provides an axially symmetric environment which reduces the complexity of the fields present in the guide.

Most waveguide measurements use the Transmission/Reflection (TR) method to extract the material parameters from the sample. This method utilizes a Network Analyzer (NWA) to measure the scattering parameters of the material contained in the waveguide. An algorithm such as Nicolson-Ross-Weir (NRW) is widely used by the TR method as a closed form method to extract the material properties from the measured scattering parameters [15-16]. The fundamental assumption of the NRW algorithm is that the material sample fully fills the cross section of the guide which restricts the fields in the system to a single dominant mode.

Typically, samples are machined which radially fill the line and have a relatively small thickness or length. At low frequencies, the wavelengths of electromagnetic waves can become very large. For example, the wavelength of an electromagnetic wave at 100 MHz is approximately 3 meters. Typically, most samples are machined to be no more than a few inches thick; therefore, they appear very “electrically thin” to low frequency incident waves. One way to practically lengthen the sample to accommodate for this electrical thinness is to manufacture thicker but less radially wide samples. This longer sample allows for more of the low frequency wave to impact the sample theoretically

improving the accuracy returned by the scattering parameters. One major downside of this approach is the introduction of radial air gaps between the inner or outer conductors.

Air gaps, such as those in the setup shown in Figure 1.1, cause the excitation of higher order modes which invalidates the single dominant mode assumption made by the NRW algorithm. Energy from the incident mode is coupled into these higher order modes at the material interface, most of which are highly evanescent. These higher order modes are scattered back and transmitted through the material to the opposite side. The detection ports of the NWA measure only the dominant mode; therefore, the energy coupled into the higher order modes is not accounted for in the reported scattering parameters. In this case, a closed form solution such as the NRW algorithm may result in dramatic errors in the extracted properties due to the unaccounted energy resident in the higher order modes.

This primary approach considered by this thesis is to perform a modal analysis of the system to produce theoretical scattering parameters which account for the energy coupled into the higher order modes. These theoretical values are used along with the measured values to determine the actual permittivity and permeability values of the material. Other approximate methods such as a perturbation analysis or closed form correction factors have shown promise in previous air gap research and may also be worthy avenues of pursuit. The details of the modal method and other possible methods are discussed in detail later in Chapter 3.

1.2 Limitations

The TR method is very useful in determining the complex permittivity and permeability of a material. For each unknown, one independent measurement is required; therefore, to determine both permittivity and permeability, two independent measurements are required. Typically, the two independent measurements used are the Reflection (S_{11}) and Transmission (S_{21}) coefficients. In the system shown in Figure 1.1, the thin material fills only a very small portion of the cross sectional area of the coaxial line. In this case, a strong reflection response from the material is not expected due to the small cross section of material to perturb the field. In the event that the reflection response is inadequate to accurately perform the modal analysis technique, an additional independent S_{21} measurement is needed to provide the necessary equations to determine both parameters of interest. An independent S_{21} measurement may be obtained by measuring samples of varying lengths or radial thickness.

An additional limitation of this research is the availability of accurate, well quantified, permittivity values for the WaveX material used in the measurements. Some WaveX measurements have been conducted by the Georgia Tech Research Institute (GTRI) and provide permittivity and permeability data for varying frequency ranges. Neither set of measurements are statistically well quantified, as the reported properties for different samples may vary extensively. It is anticipated that the results from the modal method utilized in this research will coincide with the measured values from GTRI shown in Appendix D within a reasonable margin of difference.

1.3 Scope

Other methods, such as microstrip probes could be used to approach the problem of low frequency measurements of thin materials. Previous research developed the Full Wave Modal Method for a coaxial transmission line with inner or outer air gaps [8]. This thesis builds upon this method and its effectiveness in extracting the complex permittivity and/or permeability of very thin dielectric and magnetic materials from the measured scattering parameters. The method is verified first using samples of a low loss dielectric material and then expanded to a lossy magnetic material. The magnetic material (WaveX WX-A020) is 20 mils thick and is specifically designed for EMI absorption at low frequencies. Considering the possible limitation of the S_{11} measurement described in Section 1.2, multiple length samples were used to obtain independent S_{21} measurements. The lower bound of the frequency range is set to 50 MHz which is slightly above the 10 MHz lower bound of the Network Analyzer. In theory, the modal method should prove valid for all frequency ranges at which measurements can be conducted. Other methods such as striplines, perturbation techniques, and air gap corrections may be investigated for purposes of comparison to the coaxial line modal method.

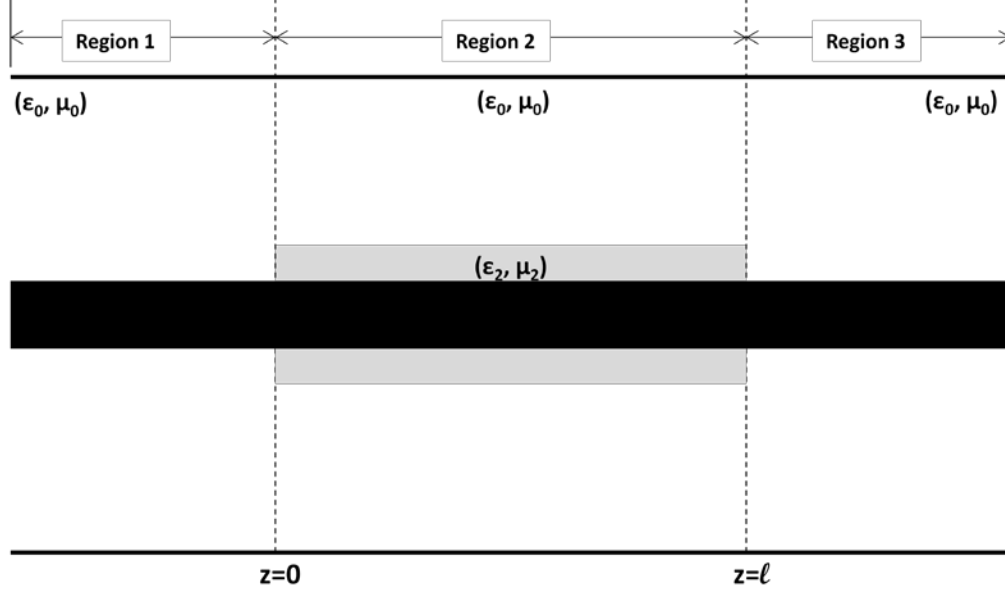


Figure 1.1: Low Frequency Coaxial Transmission Line Concept

1.4 Thesis Organization

Chapter 2 contains an overview of electromagnetic fundamentals starting with Maxwell's equations and moves through the wave equation and the development of the potential function which is the basis for the determination of the fields in the waveguide. It also contains an overview of the field development for the partially filled region and discusses previous research efforts which focused on the correction of air gaps for the waveguide TR method. Chapter 3 highlights the development of the Full Wave Modal Method for the partially filled coaxial line and discusses the experimental setup scenarios for material parameter extraction. This chapter also briefly discusses other methods for solving the low frequency problem. Chapter 4 presents the experimental results and discusses the potential sources of errors resulting from this method. Chapter 5 concludes the thesis with a summary of the effort and recommendations for future research.

II. BACKGROUND

This chapter contains the background for the characterization of thin samples in a TEM coaxial transmission line using the Full Wave Modal Method developed in Chapter 3. The terms waveguide and transmission line are used interchangeably throughout the document. Wrapping a thin sample of material around either the inner or outer conductor of a coaxial line presents a unique challenge to account for the air-gap errors introduced by the excitation of higher order modes in the system. Previous research efforts focused on solving the air gap problem using varying methods and this thesis focuses on the application of the modal method to very thin samples of high-loss magnetic material in the TEM coaxial line shown in Figure 2.1.

2.1 Transmission/Reflection (TR) Method and Coaxial Waveguides

The Coaxial Air-Line method is one of the most widely used means to determine the permittivity and permeability of a sample material. In this method, a sample is inserted between the inner and outer conductors. Coaxial transmission lines come in a variety of sizes which are usually precisely designed to have a characteristic impedance of 50Ω . This impedance is determined from the formula

$$Z_c = \frac{60}{\sqrt{\epsilon_r}} \ln\left(\frac{c}{a}\right)$$

where ϵ_r is the relative dielectric permittivity of the insulating material between the inner and outer conductors (usually air) and a and c are the respective radii of the inner and outer conductors. Most Network Analyzers have a characteristic impedance of 50Ω , so

most transmission lines are designed to match this value. In theory, a coaxial transmission line has a lower operating frequency range of 0 Hz giving it a wide operating frequency range and making it an ideal method for low frequency measurements. Typically the coaxial lines are named based on their outer diameter and Table 2.1 gives examples of several 50Ω coaxial lines and their approximate working frequency range [5]. The 14mm coaxial line used in this research had inner and outer conductor radii of 0.122" and 0.281" respectively.

The TR method of material characterization is widely employed because it produces closed-form solutions for the determination of complex permittivity and permeability which are based on the measured scattering parameters of the sample. In a coaxial line, an incident (usually TEM) wave is introduced on the system by a Network Analyzer which interacts with a sample that fully fills the cross-sectional area of the sample holder as shown in Figure 2.2 (a). The sample will reflect a portion of the field back to Port 1 of the NWA which in turn measures this reflected energy and calculates the scattering parameter S_{11} , also known as the reflection coefficient. The remaining portion of the energy will be either absorbed and/or transmitted through the sample and the NWA measures this at Port 2 and calculates S_{21} or the transmission coefficient. These two values along with the known sample length are then used in the NRW algorithm to calculate the complex permittivity and permeability of the sample using the formulas from [15-16]. Uncertainties of course can exist in this algorithm, but these have been investigated by multiple researchers and can be generally expressed as

$$\begin{aligned}
U_{\varepsilon_r'} &= \sqrt{\sum_{n=1}^N \text{Re} \left(\frac{\partial \varepsilon_r}{\partial e_i} \cdot U_{e_i} \right)^2} \\
U_{\varepsilon_r''} &= \sqrt{\sum_{n=1}^N \text{Im} \left(\frac{\partial \varepsilon_r}{\partial e_i} \cdot U_{e_i} \right)^2} \\
U_{\mu_r'} &= \sqrt{\sum_{n=1}^N \text{Re} \left(\frac{\partial \mu_r}{\partial e_i} \cdot U_{e_i} \right)^2} \\
U_{\mu_r''} &= \sqrt{\sum_{n=1}^N \text{Im} \left(\frac{\partial \mu_r}{\partial e_i} \cdot U_{e_i} \right)^2}
\end{aligned} \tag{2.1}$$

where e_i is either the amplitude of S_{11} , phase of S_{11} , amplitude of S_{21} , phase of S_{21} , and length of sample D. U_a is the uncertainty of a where the parameter a refers to the real and imaginary parts of permittivity and permeability [5].

2.2 The TEM Coaxial Waveguide

Typically, a sample of material is machined to fully fill the cross-section of the waveguide so that the NRW algorithm may be utilized to extract the material parameters. In many cases, discontinuities such as an air gap like the one shown in Figure 2.2 (b) are introduced to the system. Air gaps commonly present themselves as a result of factors

Table 2.1: Examples of different coaxial transmission lines and their working frequency range [5]. The coaxial lines are typically referenced according to their outer diameter. For this research, a 14mm coaxial line was used.

Outer Diameter (mm)	Working Frequency Range (GHz)
3.5	0 – 34.5
7.0	0 – 18.2
14.0	0 – 8.6



Figure 2.1: 14mm Coaxial Transmission Line

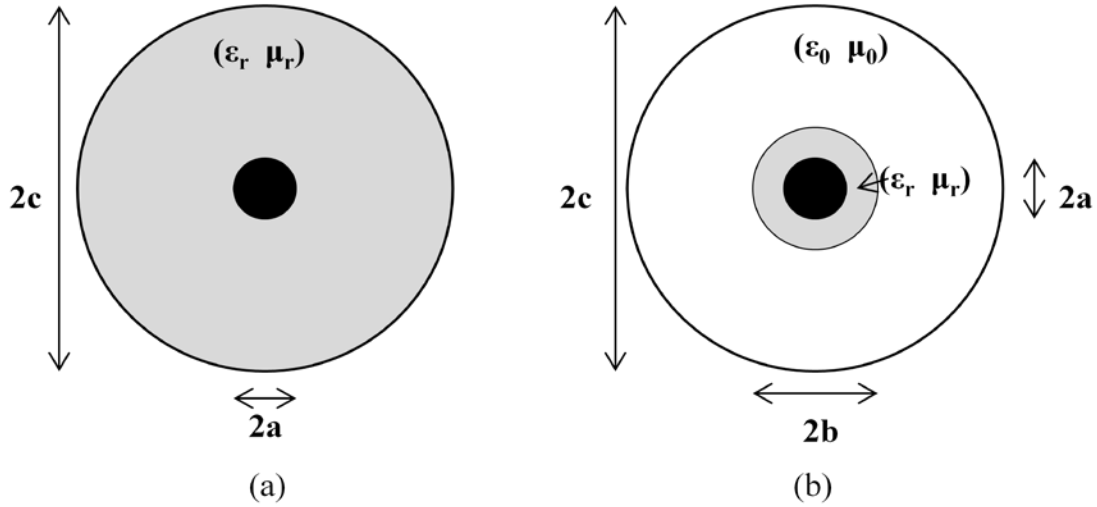


Figure 2.2: A coaxial transmission line containing a sample that (a) fully fills the cross-sectional area and (b) partially fills the cross-sectional area with a large outer airgap. Scenario (b) is the scenario considered in this research.

such as improper machining of samples, thermal contraction and expansion, and sample wear after repeated press fits over time. Typically these gaps are small and unintentional, so their effects are well documented. Air gaps are problematic because they change the fundamental field structure within the waveguide which can dramatically affect parameter extraction techniques such as the NRW algorithm. To fully understand the effects of these air gaps, a thorough knowledge of the fields in the guiding structure is required. Appendix A summarizes the development of the potential function, beginning with Maxwell's Equations, which is then used to define the fields in the line. Appendix B shows the development of the TEM and TM^z fields in the coaxial waveguide which is fully filled by free-space. In the case of the empty or fully-filled guide considered in Appendix B, the TEM mode is the dominant propagating mode in the system. Higher order TE and TM modes can exist but are typically highly evanescent and considered negligible in these cases.

In the partially filled guide as shown in Figure 2.3, a TEM mode can only propagate in the partially filled region if the \hat{z} -directed phase front remains continuous across the radial material to air gap boundary. This implies that

$$e^{-j\gamma_{air}z} = e^{-j\gamma_{mat}z} \quad (2.2)$$

where γ_{air} and γ_{mat} are the propagation constants of the wave through air and the material. In a coaxial line, the expression for the \hat{z} -directed propagation constant is

$$\gamma^2 = k_\rho^2 - k^2 \quad (2.3)$$

where $k_p = 0$ for the TEM mode. This implies that for the TEM mode, $\gamma = k$ which is the frequency dependent wavenumber of the material. In order for (2.2) to hold for the TEM mode,

$$\gamma_{air} = \gamma_{mat} \quad (2.4)$$

which requires $k_{air} = k_{mat}$. This means that the material must either be free space ($\epsilon_r, \mu_r = 1$) or have relative permittivity and permeability such that $\epsilon_r = 1/\mu_r$. The former case is impossible with a material other than air and the latter case is highly unlikely in general; therefore, a TEM mode physically will not exist in the partially filled region.

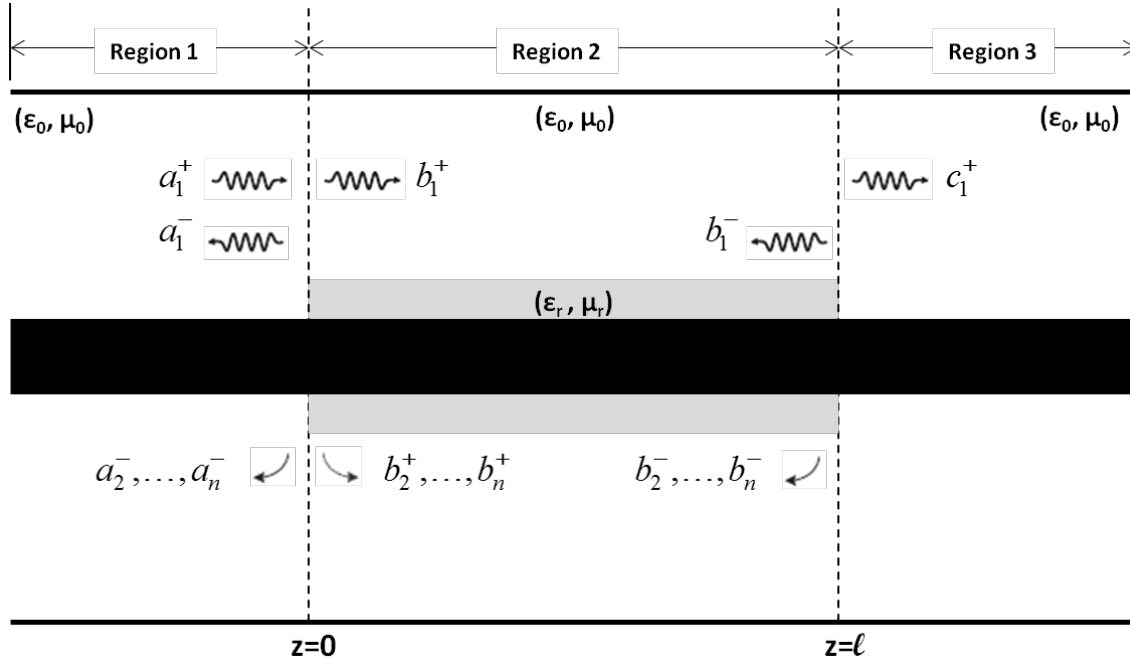


Figure 2.3: The coaxial transmission line containing a finite length sample of material which only partially fills the radial cross section of the guide

Since the TEM mode does not exist in the partially filled region, other higher order TE or TM modes must exist and propagate through the region. When the NWA measures the scattering parameters, only the dominant mode is measured. Due to the law of conservation of energy, the energy that is measured at the end of the closed system must be equal to that which is introduced to the system. Since the TEM mode does not propagate in Region II, the energy from the propagating TEM mode in Region I must couple into the higher order TE or TM modes at the region boundary. Since the NWA measurements take into account only the dominant propagating mode, the energy coupled into the higher order modes in Region II is not theoretically accounted for leading to errors in the extracted material parameters.

The first step to accounting for these errors is to determine what fields exist in the partially filled region. Assuming axial symmetry, the TE^z fields in Region II would consist of the E_ϕ, H_ρ, H_z components. The incident TEM fields from Region I consist of the E_ρ and H_ϕ components. In order for the TE modes to exist in Region II, the TEM incident fields must excite an orthogonal field (i.e. E_ρ^{TEM} must excite E_ϕ^{TE}), which for an isotropic material considered in this research is not possible. Therefore, only TM higher order modes can exist in the partially filled coaxial region.

The forward propagating TM^z fields in a general coaxial waveguide are developed in Appendix C. For the partially filled region, the \hat{z} -directed propagation constant remains the same in both materials, but the radial components of each region are unique. This fact is what allows for the extraction of the material properties of each region from the determination of the propagation constant. The axially invariant TM fields for a

region containing an outer air gap after PEC boundary conditions are applied at the inner and outer conductors are

$$E_\rho(\rho, z) = \begin{cases} \frac{k_{\rho 1n} \tilde{\gamma}_n B_{1,0n}}{j\omega \varepsilon_0 \mu_0 J_0(k_{\rho 1n} c)} W_1(k_{\rho 1n} \rho) e^{-\tilde{\gamma}_n z} & \dots \quad b < \rho < c \\ \frac{k_{\rho 2n} \tilde{\gamma}_n B_{2,0n}}{j\omega \varepsilon_2 \mu_2 J_0(k_{\rho 2n} a)} V_1(k_{\rho 2n} \rho) e^{-\tilde{\gamma}_n z} & \dots \quad a < \rho < b \end{cases}$$

$$E_z(\rho, z) = \begin{cases} \frac{k_{\rho 1n}^2 B_{1,0n}}{j\omega \varepsilon_0 \mu_0 J_0(k_{\rho 1n} c)} W_0(k_{\rho 1n} \rho) e^{-\tilde{\gamma}_n z} & \dots \quad b < \rho < c \\ \frac{k_{\rho 2n}^2 B_{2,0n}}{j\omega \varepsilon_2 \mu_2 J_0(k_{\rho 2n} a)} V_0(k_{\rho 2n} \rho) e^{-\tilde{\gamma}_n z} & \dots \quad a < \rho < b \end{cases}$$

$$H_\phi(\rho, z) = \begin{cases} \frac{k_{\rho 1n} B_{1,0n}}{\mu_0 J_0(k_{\rho 1n} c)} W_1(k_{\rho 1n} \rho) e^{-\tilde{\gamma}_n z} & \dots \quad b < \rho < c \\ \frac{k_{\rho 2n} B_{2,0n}}{\mu_2 J_0(k_{\rho 2n} a)} V_1(k_{\rho 2n} \rho) e^{-\tilde{\gamma}_n z} & \dots \quad a < \rho < b \end{cases}$$

where $\tilde{\gamma}_n = jk_z$ for the n^{th} mode and

$$\begin{aligned} V_m(\alpha\rho) &= [J_m(\alpha\rho)Y_0(\alpha a) - J_0(\alpha a)Y_m(\alpha\rho)] \\ W_m(\alpha\rho) &= [J_m(\alpha\rho)Y_0(\alpha c) - J_0(\alpha c)Y_m(\alpha\rho)]. \end{aligned} \quad (2.5)$$

The next boundary condition which must be enforced is the continuity of tangential electric and magnetic fields across the material interface in the region. When evaluated at the material to air interface at $\rho = b$, the tangential \vec{E} and \vec{H} fields in each region are equal. This implies that

$$\begin{aligned} E_z(b^-) &= E_z(b^+) \\ H_\phi(b^-) &= H_\phi(b^+). \end{aligned}$$

Solving both equations for the constant $B_{2,0n}$ yields

$$B_{2,0n} = B_{1,0n} \frac{k_{\rho 1n}^2 \varepsilon_2 \mu_2 J_0(k_{\rho 2n} a) W_0(k_{\rho 1n} b)}{k_{\rho 2n}^2 \varepsilon_0 \mu_0 J_0(k_{\rho 1n} c) V_0(k_{\rho 2n} b)}$$

$$B_{2,0n} = B_{1,0n} \frac{k_{\rho 1n} \mu_2 J_0(k_{\rho 2n} a) W_1(k_{\rho 1n} b)}{k_{\rho 2n} \mu_0 J_0(k_{\rho 1n} c) V_1(k_{\rho 2n} b)},$$

which when equated produces the characteristic equation for $\tilde{\gamma}_n$

$$k_{\rho 1n} \varepsilon_2 V_1(k_{\rho 2n} b) W_0(k_{\rho 1n} b) - k_{\rho 2n} \varepsilon_0 V_0(k_{\rho 2n} b) W_1(k_{\rho 1n} b) = 0 \quad (2.6)$$

where

$$k_{\rho 1n} = \sqrt{\tilde{\gamma}_n^2 + k_0^2} \text{ and } k_{\rho 2n} = \sqrt{\tilde{\gamma}_n^2 + k_2^2}.$$

Equation (2.6) must be solved for its complex roots, of which there are an infinite number. This cannot be solved analytically; therefore, a numerical method is needed to find the roots. Methods such as the Gauss-Newton or Levenberg-Marquardt methods are commonly used algorithms to solve equations of this type. Care must be taken to ensure that the solutions returned correspond to the correct mode, since for magnetic materials the wavenumbers are not necessarily sequential (i.e. decreasing complex components with increasing real components).

2.3 Air Gap Correction Efforts

Closed form solutions such as the NRW algorithm are the preferred method to recover a material's permittivity and permeability due to their simplicity. As discussed previously, these solutions have significant drawbacks when being used in environments which contain higher order modes. Significant prior research has been conducted

detailing attempts to derive air gap correction factors for use with methods such as NRW. A few of these methods include the Lumped Capacitor and Inductor model developed by the National Institute of Standards and Technology (NIST) [1] and the full wave modal method performed in [8].

2.3.1 Circuit Model Corrections. The correction factors developed by NIST assume a single dominant mode in the system, which for very small air gaps is a relatively good assumption. For the correction of permittivity, the partially filled line is treated as a system of capacitors in series using the dimensions for the general case of an inner and outer air gap shown in Figure 2.4 so that

$$\frac{1}{C_m} = \frac{1}{C_1} + \frac{1}{C_2} + \frac{1}{C_3}. \quad (2.7)$$

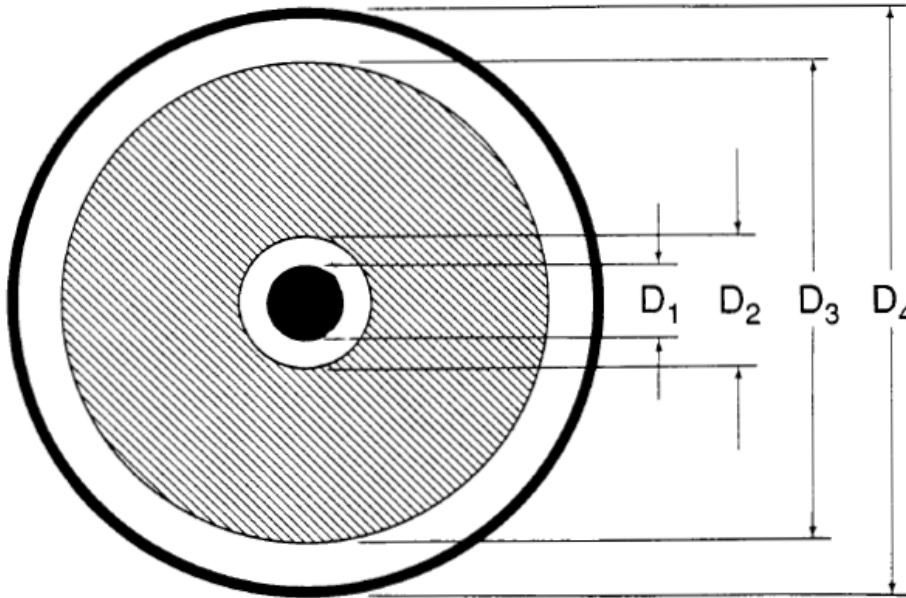


Figure 2.4: Partially Filled Coaxial Line with Inner and Outer Air Gaps

The electric field distribution for a coaxial line is given by

$$E_\rho = \frac{V}{\ln\left(\frac{c}{a}\right)\rho},$$

where a and c correspond to the inner and outer conductor radius. The voltage between the conductors is rigorously defined as

$$V = - \int_{(-)}^{(+)} \vec{E} \cdot d\vec{l}.$$

and the capacitance of the coaxial line with length L is given by

$$C = \frac{2\pi\epsilon L}{\ln\left(\frac{R_2}{R_1}\right)}.$$

where R represents the appropriate radii from Figure 2.4. The system of capacitors described in (2.7) is defined as

$$\frac{\ln\left(\frac{R_4}{R_1}\right)}{\epsilon'_m} = \frac{\ln\left(\frac{R_2}{R_1}\right)}{\epsilon'_1} + \frac{\ln\left(\frac{R_3}{R_2}\right)}{\epsilon'_c} + \frac{\ln\left(\frac{R_4}{R_3}\right)}{\epsilon'_1} \quad (2.8)$$

where ϵ'_c, ϵ'_m are the corrected and measured real part of the sample's permittivity and ϵ'_1 is the real part of the permittivity of air. This yields the following corrections for the real and imaginary parts of the sample's permittivity:

$$\begin{aligned} \epsilon'_{cR} &= \frac{L_2(\epsilon'_{mR}L_3 - \epsilon''_{mR}L_1 - \epsilon'_{mR}L_1)}{\epsilon'^2_{mR}L_1^2 - 2\epsilon'_{mR}L_1L_3 + \epsilon''^2_{mR}L_1^2 + L_3^2} \\ \epsilon''_{cR} &= \frac{L_2L_3\epsilon''_{mR}}{\epsilon'^2_{mR}L_1^2 - 2\epsilon'_{mR}L_1L_3 + \epsilon''^2_{mR}L_1^2 + L_3^2} \end{aligned} \quad (2.9)$$

where

$$\begin{aligned}
L_1 &= \ln\left(\frac{R_2}{R_1}\right) + \ln\left(\frac{R_4}{R_3}\right) \\
L_2 &= \ln\left(\frac{R_3}{R_2}\right) \\
L_3 &= \ln\left(\frac{R_4}{R_1}\right).
\end{aligned} \tag{2.10}$$

The permeability correction is obtained by modeling the line as a series of inductors such that

$$L_m = L_c + L_{air}. \tag{2.11}$$

After analyzing the flux and solving for the inductance, the corrections for the real and imaginary parts of permeability are

$$\begin{aligned}
\mu'_{cR} &= \frac{\mu'_{mR} L_3 - L_1}{L_2} \\
\mu''_{cR} &= \mu''_{mR} \frac{L_3}{L_2}.
\end{aligned} \tag{2.12}$$

Typically, the corrected values for permeability are much less accurate than those for the permittivity since H_ϕ is continuous across the material to air boundary while E_ρ is not. The permittivity corrections in (2.9) also break down when in the case of large air gaps ($\epsilon'_{mR} \geq (L_3/L_1)$). While providing somewhat more accurate values in many cases, these correction factors are still very simplistic and based exclusively on the physical dimensions of the line and air gaps. The results of the uncorrected NRW method and the NIST corrected method for the unknown dielectric and WaveX materials are shown in Figures 2.5 and 2.6 respectively. As expected, the results returned by the NRW algorithm for both materials are poor. The corrected value for ϵ'_r of the dielectric material is overestimated but tends to follow the general trend of the fully filled scenario.

The corrected values of the WaveX measurements appear to correct the permeability closer towards the actual values. The corrected permittivity values are quite poor until after 1.5 GHz. A more exact solution requires consideration of the contributions from these higher order propagating modes present within the line. Some efforts approach the problem using perturbation techniques assuming a slight change in the fields of an otherwise fully filled line [10]. These perturbation techniques can be good estimates but still lack the rigor of other more exact methods. Other methods use correction formulas such as those examined in [4]. A rigorous method that has shown some success for dielectrics and magnetic materials with air gaps is the modal analysis or mode-matching technique.

2.3.2 Modal Analysis. The modal analysis method is a direct method which conforms close to physical reality by choosing the amplitudes of normal modes to satisfy boundary conditions at a discontinuity. Wexler [17] was one of the early pioneers of this method which allows for the interaction effects of dominant and higher-order modes between discontinuities in a rectangular waveguide to study finite length obstructions. Modal analysis considers an infinite number of higher order modes, truncated to a finite number for computational purposes, which are then summed together and lead to the formation of the readily solvable linear algebra equation

$$\overline{A}x = \overline{b}.$$

The matrix \overline{A} contains the coupling between field modes, x is a vector of unknowns which contains the theoretical reflection and transmission coefficients, and \overline{b} is the forcing vector which contains the known values from the coupling of the incident fields from Region I. The reflection and transmission coefficients correspond to the theoretical

S_{11}^{thy} and S_{21}^{thy} respectively. These values are compared to the experimentally measured scattering parameters in the form of

$$\begin{aligned} \left| S_{11}^{\text{thy}}(\omega, \varepsilon, \mu) - S_{11}^{\text{exp}}(\omega) \right| &< \delta \\ \left| S_{21}^{\text{thy}}(\omega, \varepsilon, \mu) - S_{21}^{\text{exp}}(\omega) \right| &< \delta \end{aligned} \quad (2.13)$$

where δ is the specified tolerance. A root search algorithm is used to iterate the values of permittivity and permeability in the theoretical calculation until (2.13) is true within the tolerance δ .

A large body of research has focused on this method, extending its applications to many different materials and environments [9, 18]. One such effort upon which this research is based is the application of the modal analysis technique to a partially filled coaxial transmission line.

In [8], Fehlen investigated the scenario of a TEM coaxial line partially filled with a linear, isotropic and homogenous material using the mode-matching approach. Both non-magnetic and magnetic materials were investigated for inner and outer air-gap scenarios considering a varying number of higher order modes. In the freespace filled coaxial line used in his work, he found that 32% of the electric field component of a TEM wave was concentrated in the first 2.54mm extending radially from the center conductor while only 17% of the potential was contained in the outer 2.54mm. This concludes that an inner air gap prevents a large portion of the potential from interrogating the sample. The inner air gap likely leads to increased errors in the measurements, especially in the case of a very large radial air gap. As expected, the modal method produced more accurate results when utilized with the outer airgap due to the concentration of the

electric field around the center conductor. Also, the inner air gap is more likely to induce a drooping effect where the sample loses its axial symmetry due to the lack of support from the center conductor. This elimination of symmetry precludes the use of the corrections in (2.9) and (2.12) [5]. The modal analysis technique returns good results for both materials although the inner air gap scenario proved to be less accurate, particularly for a magnetic material. The results for the MagRAM sample with a 9 mil inner or outer gap considering 10 modes is shown in Figure 2.7. As expected, the outer gap scenario with 10 higher order modes returned results that agree well with the fully filled case. The detailed development of the coaxial line modal method is summarized in Chapter 3.

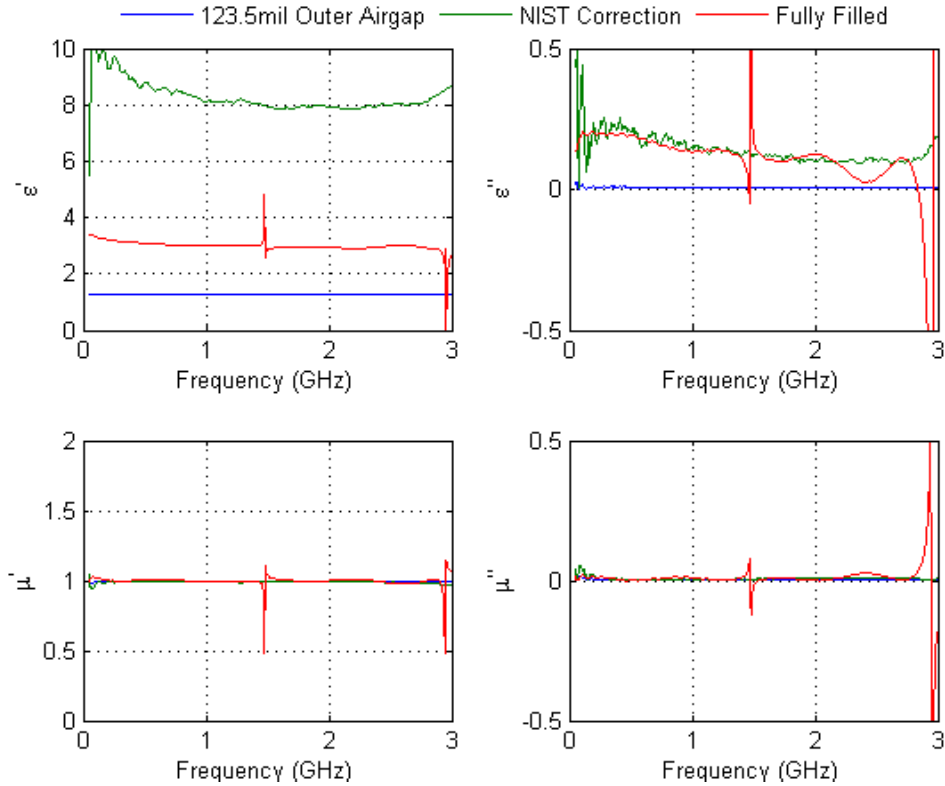


Figure 2.5: Extracted complex ϵ_r and μ_r of an unknown dielectric sample with a 123.5 mil outer air gap using the NRW algorithm and NIST correction formulas

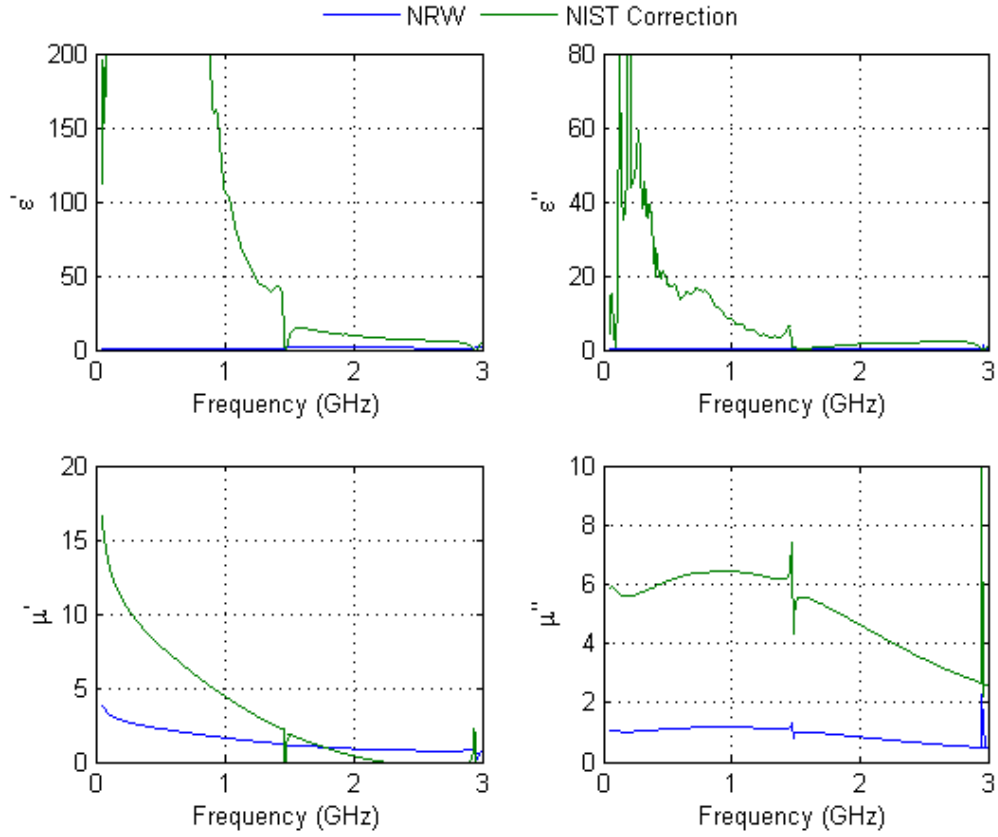


Figure 2.6: Extracted complex ϵ_r and μ_r of a WaveX sample with 139 mil outer as gap using the NRW algorithm and NIST correction formulas. The sample is wrapped around the inner conductor and radially fills approximately 12.5% of the space between the inner and outer conductors. The singular behaviors at 1.48 GHz and 2.95 GHz is assumed to be an error in calibration. The corrected μ_r values appear reasonable across the range while the corrected ϵ_r values don't appear reasonable until after 1.5 GHz.

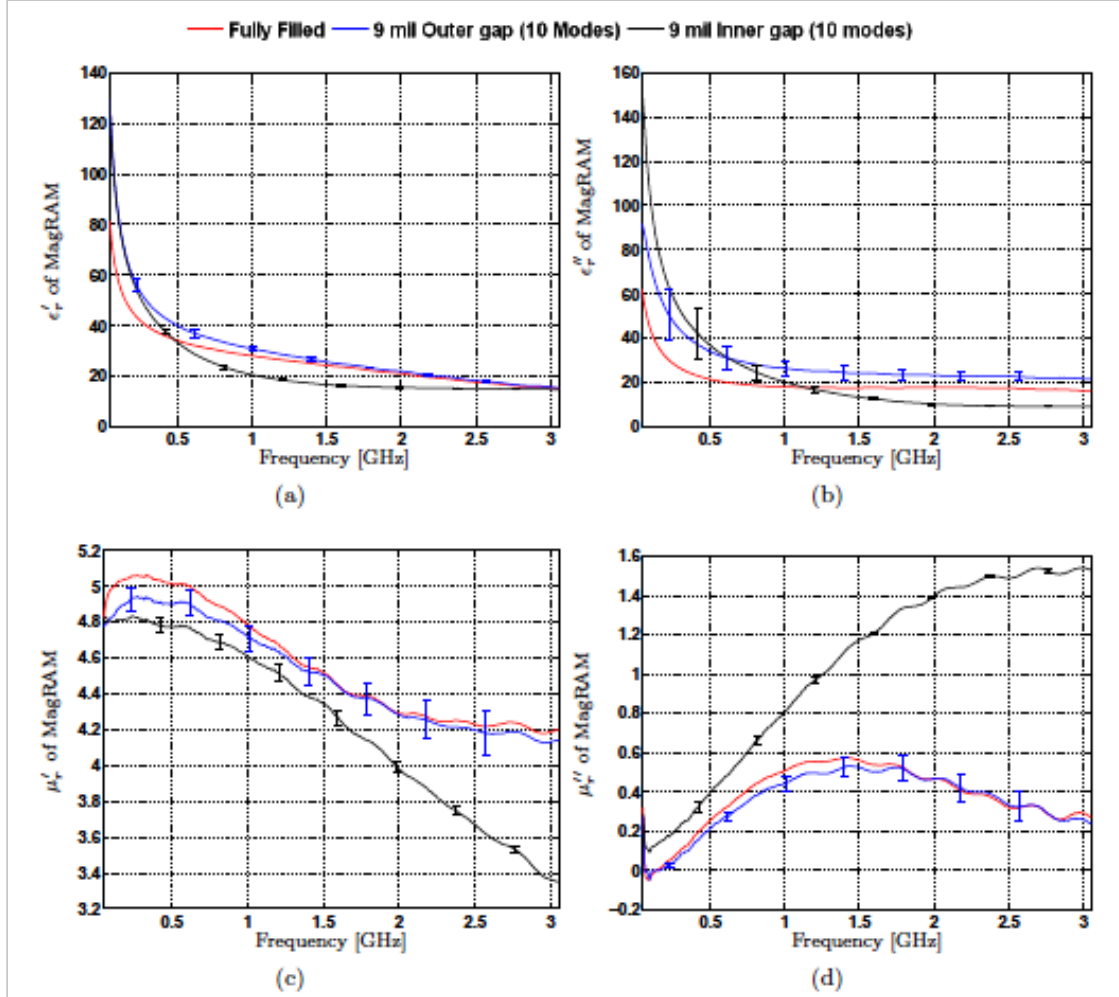


Figure 2.7: Measured complex permittivity and permeability of MagRAM samples as recorded in [8]. The modal method with 10 considered modes was used to provide accurate corrections for both the permittivity and permeability of the MagRAM.

2.4 Numerical Root Searching

The mode-matching technique is a numerical technique which relies on root searching algorithms to determine the appropriate values of permittivity and permeability to satisfy the relations in (2.13). There are many different root searching techniques which may be used; however, two of the more widely used methods are the Gauss-

Newton and Levenberg-Marquardt (LM) methods for the solution of non-linear least squares. The advantage to the Gauss-Newton method is that its rate of convergence can approach quadratic; however, it requires a relatively accurate initial guess. A poor initial guess can result in failure for the method to converge to the actual solution.

The benefit of the LM method is that it ensures the solution will eventually converge, regardless of the accuracy of the initial guess. It converges because when the initial solution is far away from the correct solution it behaves like the method of steepest descent which ensures a slow, but guaranteed convergence. As the method approaches the correct solution, it behaves like the Gauss-Newton method which quickly converges to the final solution. The LM method is slower than Gauss-Newton, but more robust and is a good choice when an accurate initial guess is not known [12, 14]. In [8], well quantified samples of Rexolite and MagRAM were measured, so a combination of Gauss-Newton and Muller complex root search algorithms were used. The WaveX material investigated in this research is not well quantified leading to the selection of the LM method due to the lack of an accurate initial guess.

2.5 Summary

Observations from previous research show that the lumped circuit model corrections defined in [1] perform reasonably well for dielectric materials but quite poorly for heavily loaded magnetic material samples in the partially filled region. Additionally, these corrections depend primarily on the size of the airgap, becoming increasingly less effective as the gap size increases. The mode-matching technique used in [8] returned accurate results for non-magnetic materials filling only 30% of the cross

sectional area, especially when considering an outer airgap scenario. Good results for high-dielectric constant magnetic material were also obtained using this method. The focus of this research is to extend this partially filled coaxial line modal analysis technique to large radial air gap scenarios containing samples of the WaveX material.

III. METHODOLOGY

The partially filled TEM coaxial transmission line excites higher order modes in the regions containing air gaps, requiring a method to account for the energy coupled into these higher order modes. The full wave modal method for this scenario was previously developed and applied in [8] to a system containing small air gaps around either the inner or outer conductor. This method obtained theoretical values for the scattering parameters S_{11}^{thy} and S_{21}^{thy} for a measured air gap size which were then compared to the measured values S_{11}^{exp} and S_{21}^{exp} using

$$\begin{aligned} \left| S_{11}^{thy}(\omega, \varepsilon, \mu) - S_{11}^{exp}(\omega) \right| &< \delta \\ \left| S_{21}^{thy}(\omega, \varepsilon, \mu) - S_{21}^{exp}(\omega) \right| &< \delta \end{aligned} \quad (3.1)$$

to extract the permittivity and permeability of the material sample. This method was experimentally verified to produce accurate results for both a dielectric (Rexolite) and magnetic (MagRAM) material after 10 modes. This section contains a summary of the development of the TEM coaxial line modal method which describes the relationship between the fields within the three regions of figure 3.1. It also highlights the unique factors considered by this research for very thin material samples.

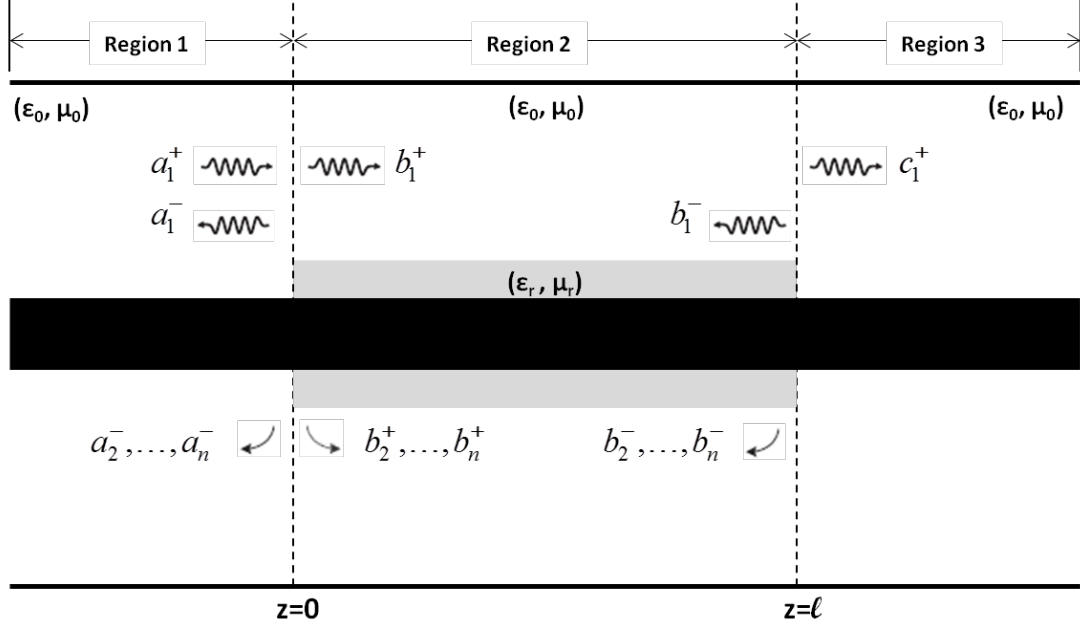


Figure 3.1: The dominant TEM mode from Region 1 couples into higher order modes in Region II excited by the air gap discontinuity. These Region 2 modes couple back into a TEM mode which propagates in Region 3 to the Port 2 detector of the NWA.

3.1 Modal Method Development for TEM Coaxial Transmission Line

There are three main steps to develop the full wave modal method. These three steps are:

1. Determine the potential modes in the system and define the fields,
2. apply boundary conditions at the interfaces to ensure a unique solution,
3. and select and apply a testing operator to generate a linear system of equations.

As discussed in Chapter 2, the partially filled TEM coaxial transmission line contains both a dominant TEM mode and higher order TM^z modes. The TEM mode only exists in the free-space filled Regions I and III whereas the higher order TM^z modes exist in all three regions. The TEM and TM^z field summaries for Regions I and III are developed in Appendix C, and considering only the forward propagating fields are summarized as

$$\begin{aligned}
E_{\rho,n} &= \begin{cases} \Upsilon \left[\frac{1}{\rho} \right] e^{-jkz} & \dots \text{TEM} \\ \frac{k_{\rho n} \gamma_n B_{0n}}{j\omega \epsilon \mu J_0(k_{\rho n} a)} V_1(k_{\rho n} \rho) e^{-\gamma_n z} & \dots \text{TM}^z \end{cases} \\
E_{z,n} &= \begin{cases} 0 & \dots \text{TEM} \\ \frac{k_{\rho n}^2 B_{0n}}{j\omega \epsilon \mu J_0(k_{\rho n} a)} V_0(k_{\rho n} \rho) e^{-\gamma_n z} & \dots \text{TM}^z \end{cases} \\
H_{\phi,n} &= \begin{cases} \frac{\Upsilon}{Z_{TEM}} \left[\frac{1}{\rho} \right] e^{-jkz} & \dots \text{TEM} \\ \frac{k_{\rho n} B_{0n}}{\mu J_0(k_{\rho n} a)} V_1(k_{\rho n} \rho) e^{-\gamma_n z} & \dots \text{TM}^z \end{cases}
\end{aligned} \tag{3.2}$$

where

$$\Upsilon = \frac{2kB_{0n}}{\pi\omega\epsilon\mu} \quad Z_{TEM} = \sqrt{\frac{\mu_0}{\epsilon_0}}$$

and

$$V_m(\alpha\rho) = [J_m(\alpha\rho)Y_0(\alpha a) - J_0(\alpha a)Y_m(\alpha\rho)] \tag{3.3}$$

where m is either 0 or 1. The characteristic equation necessary to solve for γ_n for the

TM_{0n}^z modes is

$$[J_0(k_{\rho n} c)Y_0(k_{\rho n} a) - J_0(k_{\rho n} a)Y_0(k_{\rho n} c)] = 0 \tag{3.4}$$

where

$$k_{\rho n} = \sqrt{k_0^2 + \gamma_n^2}.$$

The TM^z fields in Region II were developed in Chapter 2 and considering only the forward traveling fields are

$$\begin{aligned}
E_{\rho,n} &= \begin{cases} \frac{k_{\rho 1n} \tilde{\gamma}_n B_{1,0n}}{j\omega \varepsilon_0 \mu_0 J_0(k_{\rho 1n} c)} W_1(k_{\rho 1n} \rho) e^{-\tilde{\gamma}_n z} & \dots \quad b < \rho < c \\ \frac{k_{\rho 2n} \tilde{\gamma}_n B_{2,0n}}{j\omega \varepsilon_2 \mu_2 J_0(k_{\rho 2n} a)} V_1(k_{\rho 2n} \rho) e^{-\tilde{\gamma}_n z} & \dots \quad a < \rho < b \end{cases} \\
E_{z,n} &= \begin{cases} \frac{k_{\rho 1n}^2 B_{1,0n}}{j\omega \varepsilon_0 \mu_0 J_0(k_{\rho 1n} c)} W_0(k_{\rho 1n} \rho) e^{-\tilde{\gamma}_n z} & \dots \quad b < \rho < c \\ \frac{k_{\rho 2n}^2 B_{2,0n}}{j\omega \varepsilon_2 \mu_2 J_0(k_{\rho 2n} a)} V_0(k_{\rho 2n} \rho) e^{-\tilde{\gamma}_n z} & \dots \quad a < \rho < b \end{cases} \quad (3.5)
\end{aligned}$$

$$H_{\phi,n} = \begin{cases} \frac{k_{\rho 1n} B_{1,0n}}{\mu_0 J_0(k_{\rho 1n} c)} W_1(k_{\rho 1n} \rho) e^{-\tilde{\gamma}_n z} & \dots \quad b < \rho < c \\ \frac{k_{\rho 2n} B_{2,0n}}{\mu_2 J_0(k_{\rho 2n} a)} V_1(k_{\rho 2n} \rho) e^{-\tilde{\gamma}_n z} & \dots \quad a < \rho < b \end{cases}$$

where

$$\begin{aligned}
V_m(\alpha \rho) &= [J_m(\alpha \rho) Y_0(\alpha a) - J_0(\alpha a) Y_m(\alpha \rho)] \\
W_m(\alpha \rho) &= [J_m(\alpha \rho) Y_0(\alpha c) - J_0(\alpha c) Y_m(\alpha \rho)] \quad (3.6)
\end{aligned}$$

and m equals 0 or 1. The characteristic equation to solve for $\tilde{\gamma}_n$ is

$$k_{\rho 1n} \varepsilon_2 V_1(k_{\rho 2n} b) W_0(k_{\rho 1n} b) - k_{\rho 2n} \varepsilon_0 V_0(k_{\rho 2n} b) W_1(k_{\rho 1n} b) = 0 \quad (3.7)$$

where

$$k_{\rho 1n} = \sqrt{\tilde{\gamma}_n^2 + k_0^2} \quad \text{and} \quad k_{\rho 2n} = \sqrt{\tilde{\gamma}_n^2 + k_2^2}.$$

Once the fields are identified, it is helpful to note that only the field components which are transverse to the direction of propagation will be utilized in the modal analysis. This is due to the application of boundary conditions at the region boundaries along the direction of propagation. In the case of the \hat{z} directed coaxial line, this means that only

the E_ρ and H_ϕ fields are used from this point forward. The total transverse fields at any point in the system are described as the superposition of each potential mode of the form

$$\begin{aligned}\bar{E}_t^\pm &= \sum_{n=1}^{\infty} a_n^\pm \bar{e}_n e^{\mp \gamma_n z} \\ \bar{H}_t^\pm &= \sum_{n=1}^{\infty} a_n^\pm \bar{h}_n e^{\mp \gamma_n z}\end{aligned}\tag{3.8}$$

where a_n^\pm represents the complex amplitudes associated with each mode and \bar{e}_n and \bar{h}_n represent the respective transverse electric and magnetic field components. Assuming the material sample is a simple media (i.e. linear, isotropic, and homogenous) means that each value of a_n^\pm is constant. The propagation of the fields are defined by the $e^{\mp \gamma_n z}$ term with a propagating wave of the form of $e^{-\gamma_n z}$ in the $+\hat{z}$ direction.

Using the forms from (3.8), the modal equations for each of the three regions must be developed. Region I contains a single forward traveling TEM mode which upon scattering from the boundary at $z=0$ will return a reflected TEM mode plus an infinite number of higher order TM^z modes. These fields are represented as

$$\left. \begin{aligned} a_1^+ e_1 e^{-\gamma_1 z} + \sum_{n=1}^{\infty} a_n^- \bar{e}_n e^{+\gamma_n z} \\ a_1^+ h_1 e^{-\gamma_1 z} - \sum_{n=1}^{\infty} a_n^- \bar{h}_n e^{+\gamma_n z} \end{aligned} \right\} z < 0 \tag{3.9}$$

where the $n=1$ mode represents the dominant TEM mode and $n>1$ represents the higher order TM modes.

As previously shown in Chapter 2, a TEM mode cannot physically propagate in Region II; therefore, the incident TEM field from Region I excites an infinite number of forward traveling TM^z modes which will then be reflected at the $z=L$ boundary. This

representation contains field vectors and amplitudes along with a unique propagation constant, all of which are different from those in Region I

$$\left. \begin{aligned} \sum_{n=1}^{\infty} b_n^+ \tilde{e}_n e^{-\tilde{\gamma}_n z} + \sum_{n=1}^{\infty} b_n^- \tilde{e}_n e^{+\tilde{\gamma}_n z} \\ \sum_{n=1}^{\infty} b_n^+ \tilde{h}_n e^{-\tilde{\gamma}_n z} - \sum_{n=1}^{\infty} b_n^- \tilde{h}_n e^{+\tilde{\gamma}_n z} \end{aligned} \right\} 0 < z < L. \quad (3.10)$$

Finally, Region III contains only forward propagating modes consisting of the dominant TEM mode plus an infinite number of higher order TM^z modes which are represented as

$$\left. \begin{aligned} \sum_{n=1}^{\infty} c_n^+ e_n e^{-\gamma_n(z-L)} \\ \sum_{n=1}^{\infty} c_n^+ h_n e^{-\gamma_n(z-L)} \end{aligned} \right\} z > L. \quad (3.11)$$

This definition contains a phase shift of $e^{\gamma_n L}$ to reference the fields to the $z=L$ boundary between Regions II and III which simplifies later calculations.

Once the fields have been identified, the next step in the process is to apply the boundary conditions at region interfaces to ensure a unique solution is maintained. The continuity of tangential fields in Region II at the material to free-space boundary was already considered in the field development summarized in (3.5). Next, the continuity of tangential fields at the $z=0$ and $z=L$ boundaries must be maintained. This requires that the transverse fields described in (3.8 – 3.10) must be appropriately equated and evaluated at the appropriate value of z . This condition produces the expressions

$$\begin{aligned}
a_1^+ e_1 + \sum_{n=1}^{\infty} a_n^- e_n &= \sum_{n=1}^{\infty} b_n^+ \tilde{e}_n + \sum_{n=1}^{\infty} b_n^- \tilde{e}_n \\
a_1^+ h_1 - \sum_{n=1}^{\infty} a_n^- h_n &= \sum_{n=1}^{\infty} b_n^+ \tilde{h}_n - \sum_{n=1}^{\infty} b_n^- \tilde{h}_n \\
\sum_{n=1}^{\infty} b_n^+ \tilde{e}_n e^{-\tilde{\gamma}_n l} + \sum_{n=1}^{\infty} b_n^- \tilde{e}_n e^{\tilde{\gamma}_n l} &= \sum_{n=1}^{\infty} c_n^+ e_n \\
\sum_{n=1}^{\infty} b_n^+ \tilde{h}_n e^{-\tilde{\gamma}_n l} - \sum_{n=1}^{\infty} b_n^- \tilde{h}_n e^{\tilde{\gamma}_n l} &= \sum_{n=1}^{\infty} c_n^+ h_n
\end{aligned} \tag{3.12}$$

which is a set of four equations necessary to solve for the unknown reflection and transmission coefficients in the system. These coefficients found by normalizing the amplitudes of the fields in each region to the incident TEM amplitude a_1^+ and can be described as

$$\begin{aligned}
R_n &= \frac{a_n^-}{a_1^+} & r_n &= \frac{b_n^-}{a_1^+} \\
t_n &= \frac{b_n^+}{a_1^+} & T_n &= \frac{c_n^+}{a_1^+}.
\end{aligned} \tag{3.13}$$

where R_n and T_n correspond respectively to S_{11} and S_{21} of the system. Filling these into the system of equations in (3.12), rearranging and truncating the series to a finite value N yields

$$\begin{aligned}
\sum_{n=1}^N R_n e_n - \sum_{n=1}^N t_n \tilde{e}_n - \sum_{n=1}^N r_n \tilde{e}_n &= -e_1 \\
\sum_{n=1}^N R_n h_n + \sum_{n=1}^N t_n \tilde{h}_n - \sum_{n=1}^N r_n \tilde{h}_n &= h_1 \\
\sum_{n=1}^N t_n \tilde{e}_n e^{-\tilde{\gamma}_n l} + \sum_{n=1}^N r_n \tilde{e}_n e^{\tilde{\gamma}_n l} - \sum_{n=1}^N T_n e_n &= 0 \\
\sum_{n=1}^N t_n \tilde{h}_n e^{-\tilde{\gamma}_n l} - \sum_{n=1}^N r_n \tilde{h}_n e^{\tilde{\gamma}_n l} - \sum_{n=1}^N T_n h_n &= 0
\end{aligned} \tag{3.14}$$

which is now a system of 4 equations necessary with 4N unknowns. Considering only the $n=1$ mode, this system is well-posed and solvable for the transmission and reflection coefficients; however, the effect of higher order ($n>1$) modes cannot be considered by (3.14).

In order to consider the effects of the higher order modes on the transmission and reflection coefficients, the system of equations in (3.14) must be expanded to include 4N equations with 4N unknowns. To accomplish this, a testing operator which does not alter the parameter definitions must be applied to the system of equations. As noted by Fehlen, the Region I fields serve as ideal testing operators since the coupling between the field modes is determined by multiplying the fields together and integrating over the cross-section of the coaxial line. The scattering parameters remain constant over the surface integral, so the testing operator does not impact these parameters. A benefit of choosing the Region I fields for the testing operator is the orthogonality of fields in a fully free-space filled region such as Regions I and III. This means that for $m \neq n$ the fields do not couple into each other, reducing these integrals into a set of simplified diagonal matrices. The Region I and II fields are not orthogonal; therefore, a full set of 4N x 4N matrices will be formed accounting for all higher order mode coupling. The testing operator is applied to each term in (3.14) such as

$$\begin{aligned} \int_{CS} e_m \cdot \{ \} & \quad (m = 1, 2, \dots, N) \\ \int_{CS} h_m \cdot \{ \} & \quad (m = 1, 2, \dots, N), \end{aligned} \tag{3.15}$$

choosing the appropriate operator for the electric or magnetic field. Applying the testing operator to (3.14) yields

$$\begin{aligned}
A_{mn} &= \int_{CS} e_m \cdot e_n \, dS \\
B_{mn} &= \int_{CS} e_m \cdot \tilde{e}_n \, dS \\
C_{mn} &= \int_{CS} h_m \cdot \tilde{h}_n \, dS
\end{aligned} \tag{3.16}$$

which describe the coupling between the field coupling between regions. A separate integration to describe the magnetic field coupling between the Region I and III fields is not necessary due to the relation of the electric and magnetic fields

$$h_n = \frac{\hat{z} \times e_n}{Z_n}$$

where Z_n is the wave impedance for the nth mode. This relationship simplifies the product and integration of the testing operator fields to

$$\frac{1}{Z_m Z_n} \int_{CS} e_m \cdot e_n \, dS$$

which is simply

$$\frac{A_{mn}}{Z_m Z_n}. \tag{3.17}$$

Using the testing operator definitions from (3.16) and (3.17), the system of equations in (3.14) is rewritten as

$$\begin{pmatrix}
A_{mn} & -B_{mn} & -B_{mn} & 0 \\
\frac{A_{mn}}{Z_m Z_n} & C_{mn} & -C_{mn} & 0 \\
0 & B_{mn} e^{-\tilde{\gamma}_n l} & B_{mn} e^{\tilde{\gamma}_n l} & -A_{m,n} \\
0 & C_{mn} e^{-\tilde{\gamma}_n l} & -C_{mn} e^{\tilde{\gamma}_n l} & -\frac{A_{m,n}}{Z_m Z_n}
\end{pmatrix}
\begin{pmatrix} R_n \\ t_n \\ r_n \\ T_n \end{pmatrix} = \begin{pmatrix} -A_{m1} \\ \frac{A_{m1}}{Z_1 Z_1} \\ 0 \\ 0 \end{pmatrix} \tag{3.18}$$

where each element in the matrix is an NxN sized submatrix. Equation (3.18) is now a well posed linear system of equations readily solvable by linear algebra techniques.

The next step is to summarize the transverse fields in each region which are used in the integral calculations of the testing operators. The transverse fields for a \hat{z} directed coaxial line are the radial and axial components of the electric and magnetic fields. In the case of the particular fields for this research summarized in (3.2) and (3.5), the radial electric field (E_ρ) and axial magnetic field (H_ϕ) are the transverse fields. Normalizing these fields to the incident TEM wave by the constant

$$\Upsilon = \frac{2kB_{0,n}}{\pi\omega\epsilon\mu}$$

results in

$$\mathbf{e}_n = \begin{cases} \frac{1}{\rho} \hat{\rho} & \dots n=1 \\ \frac{\pi\gamma_n k_{\rho n}}{j2k} V_1(k_{\rho n}\rho) \hat{\rho} & \dots n>1 \end{cases} \quad (3.19)$$

$$\mathbf{h}_n = \begin{cases} \frac{1}{Z_n} \left[\frac{1}{\rho} \right] \hat{\phi} & \dots n=1 \\ \frac{\pi\gamma_n k_{\rho n}}{j2k} \left[\frac{1}{Z_n} \right] V_1(k_{\rho n}\rho) \hat{\phi} & \dots n>1. \end{cases}$$

for free-space filled Regions I and III and

$$\tilde{\mathbf{e}}_n = \begin{cases} \frac{\pi k_{\rho 2n} \tilde{\gamma}_n}{j2k_2} V_1(k_{\rho 2n} \rho) \hat{\rho} & \dots a < \rho < b \\ \frac{\pi k_{\rho 2n} \tilde{\gamma}_n}{j2k_2} \frac{\varepsilon_2}{\varepsilon_1} \frac{V_1(k_{\rho 2n} b)}{W_1(k_{\rho 1n} b)} W_1(k_{\rho 1n} \rho) \hat{\rho} & \dots b < \rho < c \end{cases} \quad (3.20)$$

$$\tilde{\mathbf{h}}_n = \begin{cases} \frac{\pi k_{\rho 2n} \tilde{\gamma}_n}{j2k_2 Z_{2n}} V_1(k_{\rho 2n} \rho) \hat{\phi} & \dots a < \rho < b \\ \frac{\pi k_{\rho 2n} \tilde{\gamma}_n}{j2k_2 Z_{2n}} \frac{V_1(k_{\rho 2n} b)}{W_1(k_{\rho 1n} b)} W_1(k_{\rho 1n} \rho) \hat{\phi} & \dots b < \rho < c. \end{cases}$$

for the partially filled Region II where

$$\begin{aligned} V_m(\alpha \rho) &= [J_m(\alpha \rho) Y_0(\alpha a) - J_0(\alpha a) Y_m(\alpha \rho)] \\ W_m(\alpha \rho) &= [J_m(\alpha \rho) Y_0(\alpha c) - J_0(\alpha c) Y_m(\alpha \rho)], \end{aligned} \quad (3.21)$$

γ_n and $\tilde{\gamma}_n$ are determined by the characteristic equations (3.4) and (3.7), and subregions 1 and 2 respectively correspond to the air-filled and material-filled portions of Region 2.

Using the fields described above, the testing operator integral calculations may be performed. The integral across the cross section of a coaxial line involves integrating along both the axial and radial components. Since this research assumes axial-invariance, the axial integral will produce a factor of 2π for each case, which is simply normalized out of all the calculations.

The coupling of the electric fields in the free-space filled Regions I and III is defined from (3.16) as

$$A_{mn} = \int_a^c \mathbf{e}_m \cdot \mathbf{e}_n \rho d\rho.$$

Knowing that fields in these regions are orthogonal to each other, only the self coupling fields ($m=n$) will produce a value other than zero. For the TEM ($m=n=1$) case,

$$\begin{aligned}
 A_{mn} &= \int_a^c e_1 \cdot e_1 \rho d\rho \\
 &= \int_a^c \left(\frac{1}{\rho} \hat{\rho} \right) \cdot \left(\frac{1}{\rho} \hat{\rho} \right) \rho d\rho \\
 &= \int_a^c \left(\frac{1}{\rho} \right) d\rho \\
 &= \ln \left(\frac{c}{a} \right)
 \end{aligned} \tag{3.22}$$

and for the TM ($m=n>1$) case,

$$\begin{aligned}
 A_{mn} &= \int_a^c \left(\frac{\pi \gamma_n k_{\rho n}}{j2k} V_1(k_{\rho n} \rho) \right)^2 \rho d\rho \\
 &= \frac{\pi \gamma_n k_{\rho n}}{j2k} \int_a^c \left(V_1(k_{\rho n} \rho) \right)^2 \rho d\rho
 \end{aligned}$$

which simplifies to

$$A_{mn} = \left(\frac{\gamma_n^2}{8k^2} \right) \left\{ 4 - c^2 \pi^2 k_{\rho n}^2 \left[V_1(k_{\rho n} c) \right]^2 \right\} \tag{3.23}$$

after recognizing

$$\begin{aligned}
 V_0(k_{\rho n} a) &= 0 && \dots \text{trivial} \\
 V_0(k_{\rho n} c) &= 0 && \dots \text{from (3.3)} \\
 V_1(k_{\rho n} a) &= \frac{2}{\pi k_{\rho n} a} && \dots \text{Wronskian relationship [3].}
 \end{aligned}$$

The mode coupling of fields from Region I to Region II are defined from (3.16) as

$$B_{mn} = \int_a^c e_m \cdot \tilde{e}_n dS$$

$$C_{mn} = \int_a^c h_m \cdot \tilde{h}_n dS.$$

These two integrals may be split based upon the radial discontinuity to form two separate integrations for each case corresponding to the fields in the material filled region and those in the air-gap region. These integrals are then summed to produce

$$B_{mn} = \int_a^b e_m \cdot \tilde{e}_n \rho d\rho + \int_b^c e_m \cdot \tilde{e}_n \rho d\rho$$

$$C_{mn} = \int_a^b h_m \cdot \tilde{h}_n \rho d\rho + \int_b^c h_m \cdot \tilde{h}_n \rho d\rho.$$
(3.24)

Each case must be analyzed for the TEM (m=1) and TM (m>1) testing operators which produce distinctly different results. The development of the integrals in (3.24) is discussed in depth in [8], and result in the following solutions:

$$B_{1n} = \frac{\pi \tilde{\gamma}_n}{j2k_2} \left[\left(\frac{k_{\rho 2n}}{k_{\rho 1n}} \right)^2 - 1 \right] V_0(k_{\rho 2n}b)$$
(3.25)

$$C_{1n} = \frac{\pi \tilde{\gamma}_n}{j2k_2 Z_n} \left[\frac{1}{Z_{1n}} \left(\frac{k_{\rho 2n}}{k_{\rho 1n}} \right) - \frac{1}{Z_{2n}} \right] V_0(k_{\rho 2n}b)$$
(3.26)

for m=1 and

$$B_{mn} = \frac{\pi \gamma_m k_{\rho m}}{j2k_0} \frac{\pi \tilde{\gamma}_n k_{\rho 2n}}{j2k_2} b \times$$

$$\left[\left(\frac{1}{k_{\rho m}^2 - k_{\rho 2n}^2} - \frac{1}{k_{\rho m}^2 - k_{\rho 1n}^2} \right) k_{\rho 2n} V_1(k_{\rho m}b) V_0(k_{\rho 2n}b) + \right.$$

$$\left. \left(\frac{\epsilon_2}{\epsilon_1 (k_{\rho m}^2 - k_{\rho 1n}^2)} - \frac{1}{k_{\rho m}^2 - k_{\rho 2n}^2} \right) k_{\rho m} V_0(k_{\rho m}b) V_1(k_{\rho 2n}b) \right]$$
(3.27)

$$C_{mn} = \frac{\pi\gamma_m k_{\rho m}}{j2k_0 Z_n} \frac{\pi\tilde{\gamma}_n k_{\rho 1n}}{j2k_1 Z_{2n}} b \times$$

$$\left[\left(\frac{1}{k_{\rho m}^2 - k_{\rho 2n}^2} - \frac{\varepsilon_1}{\varepsilon_2 (k_{\rho m}^2 - k_{\rho 1n}^2)} \right) k_{\rho 1n} V_1(k_{\rho m} b) V_0(k_{\rho 2n} b) + \right.$$

$$\left. \left(\frac{1}{k_{\rho m}^2 - k_{\rho 1n}^2} - \frac{1}{k_{\rho m}^2 - k_{\rho 2n}^2} \right) k_{\rho m} V_0(k_{\rho m} b) V_1(k_{\rho 2n} b) \right]. \quad (3.28)$$

Using the results from (3.22) through (3.28), the matrix described in (3.18) can be filled in and solved for the unknown reflection and transmission coefficients which correspond to the theoretical S_{11} and S_{21} parameters. Now, a root search algorithm may be used to solve (3.1) to return the relative complex permittivity and permeability of the material under test. As previously noted in Chapter 1, a strong reflection response is not expected due to the small thickness of the material; therefore, the S_{11} values will likely not provide a sufficient level of fidelity. To overcome this, two different length material samples should be measured and the theoretical scattering parameters for each developed using the modal method. Then, the S_{11} values from (3.1) could be replaced by a new S_{21} value independently derived from the new length sample. The comparison equation now becomes

$$\begin{aligned} \left| S_{21A}^{thy}(\omega, \varepsilon, \mu) - S_{21A}^{exp}(\omega) \right| &< \delta \\ \left| S_{21B}^{thy}(\omega, \varepsilon, \mu) - S_{21B}^{exp}(\omega) \right| &< \delta \end{aligned} \quad (3.29)$$

which contains two independently derived values of S_{21} .

3.2 Other Low Frequency Methods

In addition to the coaxial modal method, a stripline approach is briefly explored. This method is an attempt to develop an approach which can take advantage of an analytical technique such as the NRW algorithm to rapidly and accurately determine the complex permittivity and permeability of a material. The stripline easily allows for thin samples of material to be investigated making it a viable alternative to the coaxial line.

One drawback of striplines is the relative difficulty in calibration. To overcome this, a post collection calibration is accomplished. Considering the geometry shown in Figure 3.2 where Regions A and B correspond to the Port 1 and Port 2 sides of the material sample of thickness d , the measured scattering parameters relate to the scattering parameters of the material under test by

$$\begin{aligned} S_{11}^m &= S_{21}^A S_{11}^{MUT} S_{12}^A \\ S_{22}^m &= S_{12}^B S_{22}^{MUT} S_{21}^B \\ S_{21}^m &= S_{21}^A S_{21}^{MUT} S_{21}^B \\ S_{12}^m &= S_{12}^B S_{12}^{MUT} S_{12}^A. \end{aligned} \tag{3.30}$$

Rearranging the terms in (3.30) gives the S-parameters for the material under test

$$S_{11}^{MUT} = \frac{S_{11}^m}{S_{21}^A S_{12}^A} \tag{3.31}$$

$$S_{22}^{MUT} = \frac{S_{22}^m}{S_{12}^B S_{21}^B} \tag{3.32}$$

$$S_{21}^{MUT} = \frac{S_{21}^m}{S_{21}^A S_{21}^B} \tag{3.33}$$

$$S_{12}^{MUT} = \frac{S_{12}^m}{S_{12}^B S_{12}^A} \tag{3.34}$$

where S^m is the uncalibrated measured value returned by the Network Analyzer. The denominators of (3.31) - (3.34) are based upon measured results from either an air filled line or a shorted line in order to provide a calibration factor. When considering the air filled line, the sample region thickness d is assumed to be the same thickness as the MUT.

To solve for the denominators associated with the S_{21} and S_{12} values, an empty line is analyzed. Considering an arbitrary “sample-region” of thickness d , the measured S_{21} and S_{12} values of air are

$$\begin{aligned} S_{21}^{m,air} &= S_{21}^A e^{-jkd} S_{21}^B \\ S_{12}^{m,air} &= S_{12}^B e^{-jkd} S_{12}^A \end{aligned}$$

which when rearranged yield

$$\begin{aligned} S_{21}^A S_{21}^B &= S_{21}^{m,air} e^{jkd} \\ S_{12}^B S_{12}^A &= S_{12}^{m,air} e^{jkd} . \end{aligned} \tag{3.35}$$

The results from (3.35) are filled back in to (3.33) and (3.34) respectively. To solve for the unknown denominators from (3.31) and (3.32), measurements using a short are required. First, a short is inserted at $d = 0$ and S-parameters are recorded. The measured S_{11} of the short is

$$S_{11}^{m,sh} = S_{21}^A (-1) S_{12}^A$$

since the reflection coefficient of a short is simply -1. Rearranging results in

$$S_{21}^A S_{12}^A = -S_{11}^{m,sh} \tag{3.36}$$

which is used by (3.31).

The final unknown denominator ($S_{12}^B S_{21}^B$) is slightly more difficult to solve for due to phase progression issues. Considering the short has a thickness of L,

$$S_{22}^{m,sh} = S_{12}^{(B-L)} (-1) S_{21}^{(B-L)} \quad (3.37)$$

where B is the total distance from the port 1 face of the short to port 2. Knowing that

$$S_{12}^B = S_{12}^{(B-L)} S_{12}^L$$

(3.37) essentially amounts to a phase delay based on the thickness L of the short. This means that

$$S_{12}^{(B-L)} = S_{12}^B e^{jkL}.$$

An identical process is used to solve for $S_{21}^{(B-L)}$ which yields an identical phase delay of e^{jkL} . Inserting these values into (3.37) and solving for the resulting unknown $S_{12}^B S_{21}^B$ yields

$$S_{12}^B S_{21}^B = \frac{-S_{22}^{m,sh}}{e^{j2kL}} \quad (3.38)$$

which is the unknown for (3.32).

Equations (3.31) - (3.34) are then solved for the calibrated scattering parameters of the material under test. These calibrated S-parameters are then simply evaluated using the NRW algorithm for an analytical closed form solution of the complex permittivity and permeability of the material.

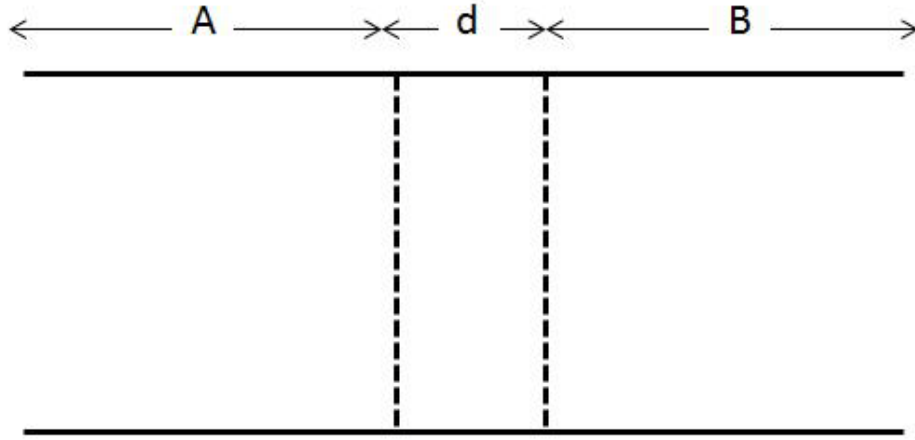


Figure 3.2: Stripline containing material sample region of arbitrary thickness d . In addition to the material sample, measurements are also taken using both air and a short as the “sample” to provide the necessary measurements to calibrate the measured data.

3.3 Summary

The modal method for a TEM coaxial transmission line is described in detail in the preceding sections. The concept of using multiple independent S_{21} measurements to solve for ϵ_r and μ_r is introduced to take the place of using both S_{11} and S_{21} values. This was developed based on the thought that thin samples containing very large air gaps would have an almost exclusive transmission component with very little scattering back towards the incident port. A method for using a low frequency transmission line to obtain calibrated scattering parameters for thin material samples is also briefly discussed.

IV. RESULTS

The modal method developed in the previous chapter was used to analyze samples which partially filled a TEM coaxial transmission line at low frequencies. This method calculates the theoretical scattering parameters S_{11}^{thy} and S_{21}^{thy} which are then compared to the measured S-parameters in a 1D or 2D complex root search. Different length samples are measured to obtain two independent transmission measurements. The additional S_{21} value may be used in place of the S_{11} parameter in the event that the measured S_{11} value is too small to accurately use to perform the minimization in equation (3.1). This is a distinct possibility given the large air gaps considered in this research preclude much if any scattering from the material sample. Like in (3.1), the theoretical values of permittivity (ϵ) and permeability (μ) are varied for each frequency step until the difference between the theoretical and measured S-parameters satisfy

$$\begin{aligned} \left| S_{21A}^{thy}(\omega, \epsilon, \mu) - S_{21A}^{exp}(\omega) \right| &< \delta \\ \left| S_{21B}^{thy}(\omega, \epsilon, \mu) - S_{21B}^{exp}(\omega) \right| &< \delta. \end{aligned} \tag{4.1}$$

4.1 Test Setup

The test setup consisted of a 14mm coaxial waveguide, an Agilent E8362B Network Analyzer and associated cables, and samples of an unknown dielectric material and the magnetic material WaveX (WX-A0X0). The dielectric samples are used to determine the effectiveness of the multiple S_{21} technique which then is applied to the WaveX samples.

The coaxial test fixture is shown broken apart in Figure 4.1 and fully assembled in Figure 4.2. The waveguide is mounted to a plate with guiding rods to ensure proper alignment each time the fixture was opened. The sample holder is inserted between the two ports and aligned via aligning pins and then secured with three tension clamps to ensure no energy leakage at the interface.

The inner conductor of the coaxial line has a radius of 122 mils and the outer conductor has a radius of 281 mils. The waveguide has three different length sample holders (880 mil, 4001 mil, and 4381 mils) with the first two used in this research. The waveguide was calibrated using a two port TRL calibration as described in [7], using the appropriate sample holder as the line standard. This sets the measurement calibration planes at the port 1 ($z=0$) and port 2 ($z=h$) faces of the sample holder. The sample lengths used for both the dielectric and WaveX ranged from 500-1500 mils which sometimes did not completely fill the sample holder lengthwise. The offsets from the calibration planes were noted and used to appropriately advance or delay the measured scattering parameters to account for the unfilled length of the sample holder.

The center conductor of the line is held in place by two “bullets” which are press fit into each end of the center conductor and mate with the corresponding Port1 and Port2 ends of the fixture. It was assumed that the center conductor remained rigidly fixed to ensure that only axially symmetric modes were excited in the sample region. A frequency sweep from 50 MHz to 3.0 GHz is conducted by collecting data at 401 discrete points along the band.

Two different sample lengths of dielectric were machined to a wall thickness of 35.5 mils, yielding a 123.5 mil outer air gap. These samples filled approximately 22.3%

of the radial surface area between inner and outer conductor. An additional dielectric sample was machined to completely fill the sample holder to determine the baseline material parameters using the NRW algorithm. This is the value that is used in comparison to the partially filled scenarios.



Figure 4.1: Coaxial Test Fixture with Sample Holder and Inner Conductor Exposed



Figure 4.2: Assembled Coaxial Test Fixture

The WaveX samples were cut from sheets of 10 mil and 20 mil thickness and then wrapped around the center conductor resulting in outer air gaps of 149 mils and 139 mils respectively. These samples respectively filled approximately 6.3% and 12.6% of the radial surface area between inner and outer conductor. The WaveX sheets contain a self-

adhesive backing which allowed them to be secured to the center conductor without the use of any tapes or pastes. The samples, once secured to the center conductor, contained slight imperfections as the samples were prepared and wrapped by hand without the use of precision machining. The most prevalent source of error in this method is likely to be in the axial plane as the edges of the material were not always completely mated. This is expected to have a greater impact on the magnetic field as it is $\hat{\phi}$ directed and will experience a slight discontinuity at the boundary. Additionally, a sample which fully fills the sample holder was crafted by wrapping multiple layers on top of each other since a machined sample was unavailable for this research. This yielded a crude sample for which the NRW algorithm could be used to extract the permittivity and permeability to get a rough baseline for comparison.

As previously mentioned, strong reflection responses were not anticipated since both materials fill less than 25% of the radial surface area. Different length samples were prepared to obtain multiple independent transmission (S_{21}) measurements. For the dielectric material, only a 1D complex root search is required to find ϵ_r since $\mu_r = 1$ is known; therefore, only one S_{21} measurement is needed. A 2D complex root search also performed for the dielectric using the measured S_{11} and S_{21} values which compares fairly well to the fully-filled and 1D solution. Since the WaveX contains both permittivity and permeability, a 2D complex root search is needed. The magnitudes of the S-parameters for the WaveX sample are shown in Figure 4.4. Since the $|S_{11}|$ for WaveX is relatively large, a root search using both S_{11} and S_{21} values could be used.

This thesis presents data obtained using S_{11} and S_{21} for the root search as well as data obtained using two independently obtained S_{21} measurements.

4.2 Modal Method Performance

The modal method was used to extract the relative permittivity and permeability from samples of a dielectric and WaveX, both of which only partially fill the waveguide resulting in large outer air gaps. The performance of the modal method for both materials is described here.

4.2.1 Performance for a thin dielectric. The modal method performed quite well for the unknown dielectric samples measured in this research. Performing a 1D root search using the measured S_{21} values, the modal method considering 20 modes was used across the entire frequency range to solve for the relative permittivity. Figure 4.3 shows the extracted permittivity values from the modal method compared to the fully filled permittivity obtained via the NRW algorithm. The modal method results clearly converge to the fully filled results after only a few frequency steps and agree well with the fully filled case across the frequency range with a couple of exceptions. The fully filled scenario consistently exhibits spikes at approximately 1.48 GHz and 2.95 GHz which are likely the frequencies that correspond to a half and full wavelength for the empty line standard during calibration.

A 2D complex root search, iterating both ϵ_r and μ_r , was then conducted using both the measured S_{11} and S_{21} values from the same dielectric sample used in the 1D case. The magnitudes of the measured S_{11} and S_{21} values are shown in figure 4.4. As

expected, the transmitted component greatly dominates the reflected component across the entire frequency range. The extracted values of ε_r and μ_r returned from the 2D search are shown in Figure 4.5. In both the 1D and 2D searches, a higher than expected value for ε_r'' was reported. This would indicate that the material is of a slightly more lossy nature than originally anticipated.

Another finding discovered for the dielectric samples is the number of modes required to achieve convergence. Figure 4.6 clearly shows that the results appear to converge after the use of only 10 modes. This finding coincides very well with the results reported in [8] for samples of Rexolite[®]. A perturbation analysis was also conducted using the method described in [10] to obtain an approximate solution for ε_r . This method considers that the permittivity of the material is only slightly perturbed from that of free space yielding an expression for ε_{MUT} of

$$\begin{aligned}\varepsilon_{MUT} &\approx \varepsilon_0(1 + \Delta\varepsilon_r) \\ &= \varepsilon_0 + \frac{j2 \ln(S_{21}^{MUT} / S_{21}^{air})}{(k_0 / \varepsilon_0)l} \frac{\ln(c / a)}{\ln(b / a)} \\ \Rightarrow \varepsilon_r &= 1 + \frac{j2 \ln(S_{21}^{MUT} / S_{21}^{air})}{(k_0 / \varepsilon_0)l} \frac{\ln(c / a)}{\ln(b / a)}.\end{aligned}$$

The comparison of the perturbation method to the fully filled case is shown in Figure 4.7. It is evident from this that the higher order modes do carry a significant enough amount of energy that they need to be included in the analysis.

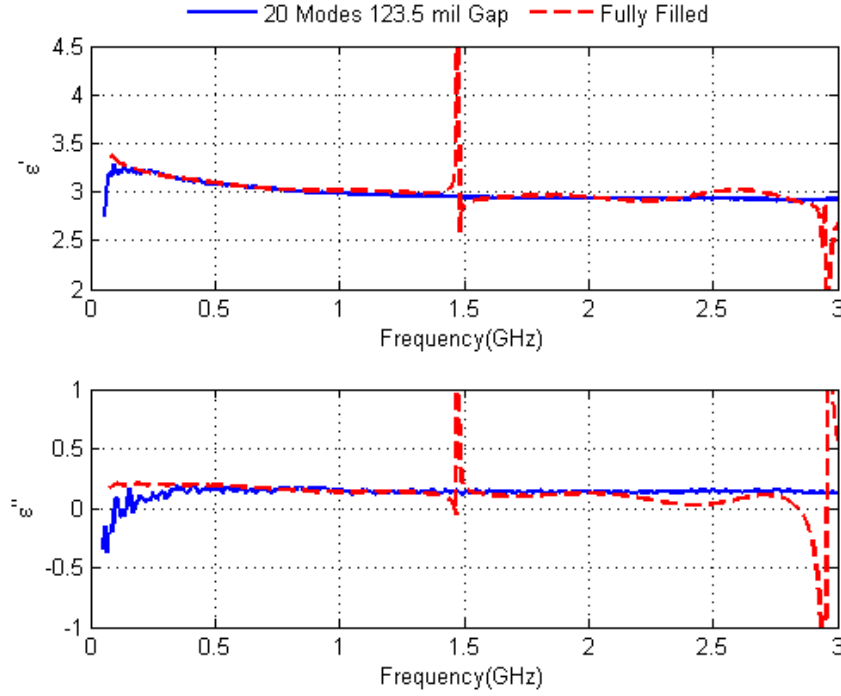


Figure 4.3: Calculated ϵ_r of a dielectric with a 123.5 mil outer air gap using 20 modes. The spikes in the Fully Filled NRW values are the result of an unidentified error in the calibration kit; otherwise, the calculated values agree very well with the fully filled values. These results were obtained from a 1D root search using S_{21} values.

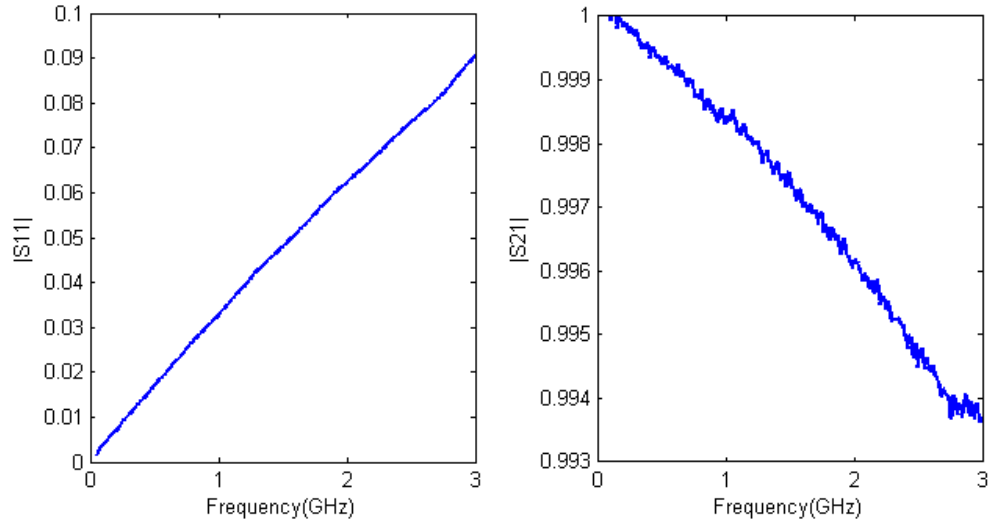


Figure 4.4: Magnitude of S_{11} and S_{21} for a 0.5" long sample of dielectric with a 123.5 mil outer air gap. As expected, $|S_{11}|$ is extremely small due to the large air gap. These magnitudes are used to perform a 2D root search to solve for ϵ_r and μ_r for the dielectric.

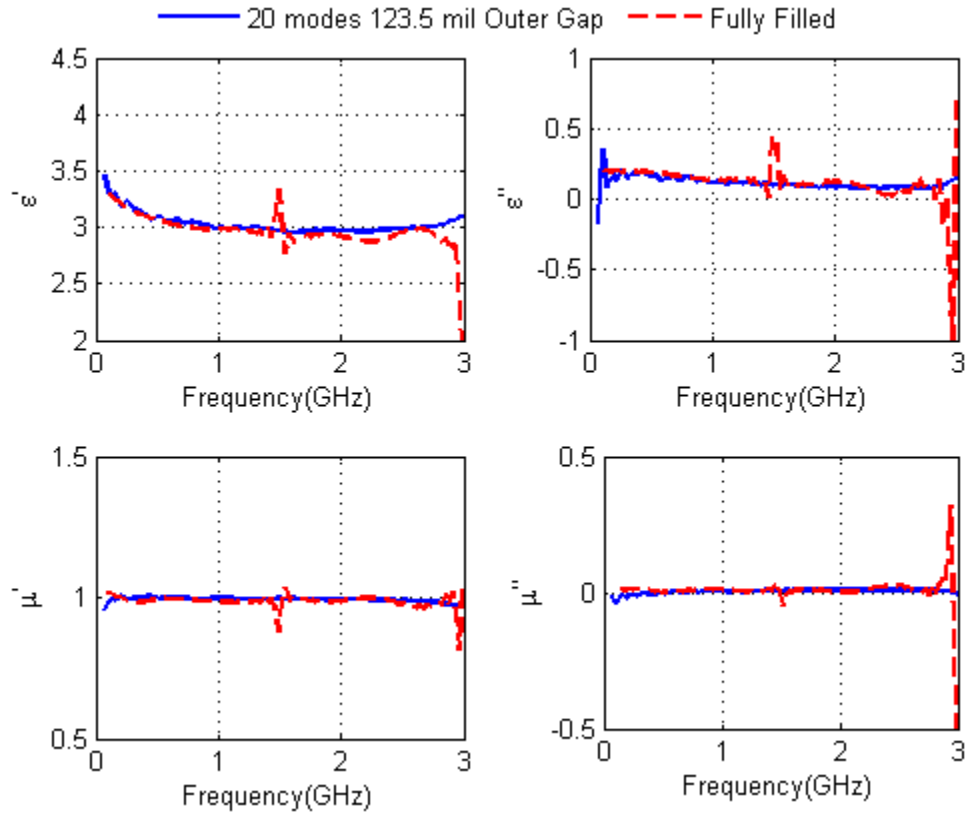


Figure 4.5: Extracted complex permittivity and permeability of a 0.5" dielectric sample with a 123.5 mil outer air gap considering 20 modes compared with the extracted values from the fully filled case. Much like the results returned from the 1D root search, the complex permittivity agrees very well with the fully filled results aside from the singularities in the fully filled case. As expected, the extracted permeability values are $\mu'_r \approx 1$ and $\mu''_r \approx 0$.

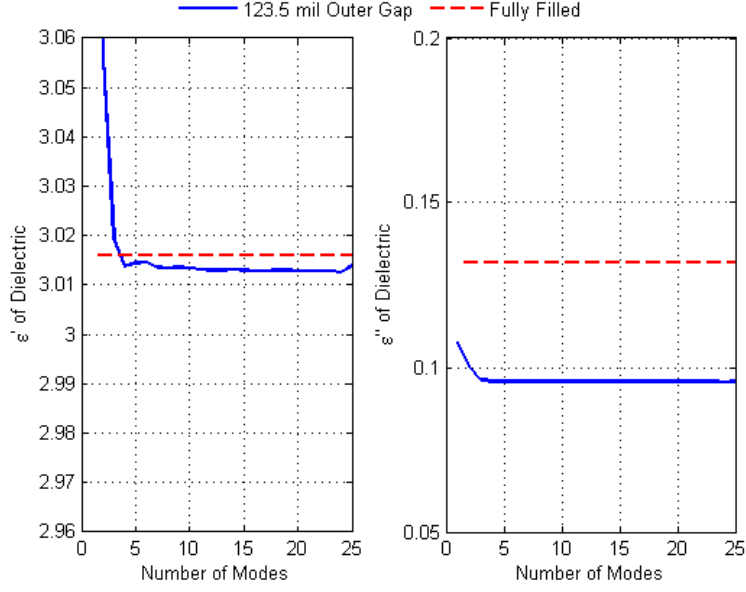


Figure 4.6: Measured complex permittivity at 1 GHz shown as $\epsilon_r = \epsilon'_r - j\epsilon''_r$. The results appear to converge after approximately 10 modes for the low dielectric constant material measured.

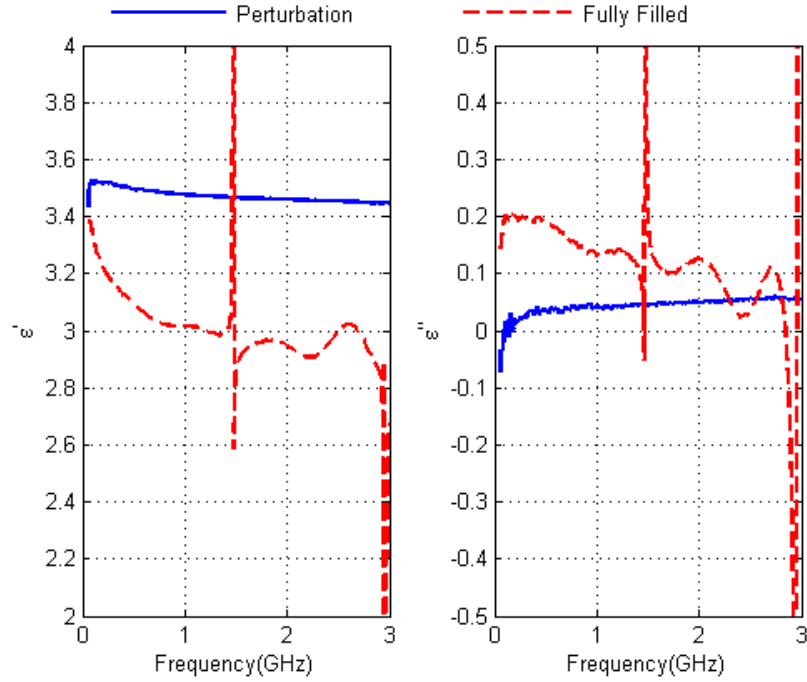


Figure 4.7: A perturbation analysis is performed as described in [10] to find the complex permittivity ϵ'_r of the dielectric. This assumes that the fields in the sample region behave like the empty guide dominant mode, only slightly perturbed by $\Delta\epsilon$.

4.2.2 *Performance for WaveX.* The modal method performed quite poorly for the samples of 20 mil thick WaveX material with a 139 mil outer air gap. A maximum of 5 modes was used in the modal analysis as the inclusion of additional higher order modes caused the algorithm to break down. As expected, the first mode excited in the sample region (TM_{00}) carries the vast majority of the energy while the other higher order modes all evanesce very rapidly as shown in Figure 4.8

The original assumption was that the magnitude of the returned S_{11} measurements would be insufficient to use in a root search, leading to a need to obtain two independent S_{21} measurements. As shown in Figure 4.8, the S_{11} magnitudes were large enough to be used, so the parameter extraction was conducted using both methods. The results from both methods are shown in Figures 4.9 and 4.10.

The extracted μ_r values surprisingly yielded relatively accurate results, but the returned values for ϵ_r were very inaccurate, particularly at the lower frequency ranges. The μ_r values agreed relatively well with the GTRI in-plane permeability shown in Figure D.3 for the “Old” sample. They also agree relatively well with the fully filled solution obtained from the crafted sample which fully filled the guide. The ϵ_r values extracted had very high, negative imaginary parts and very large real components, both of which are not readily explained. They should have agreed with the out-of-plane permeability results shown in Figure D.1. This phenomena was consistent with both approaches to the root search.

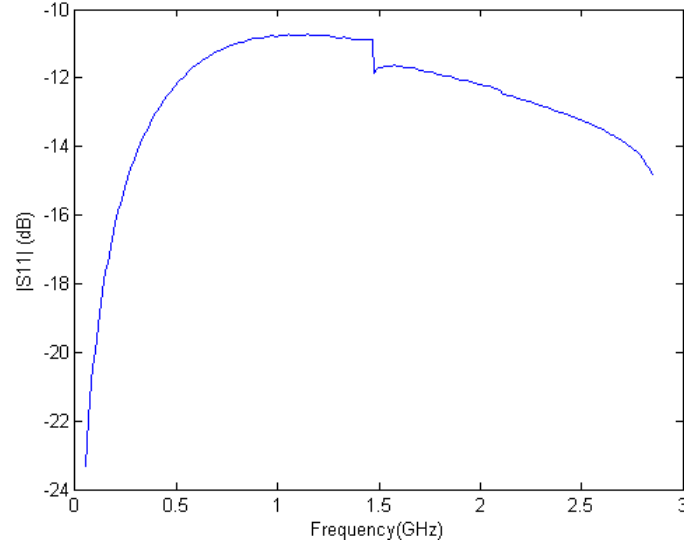


Figure 4.8: The dB magnitude of the measured S_{11} for a 1.48'' long sample of WaveX with a 139 mil outer air gap.

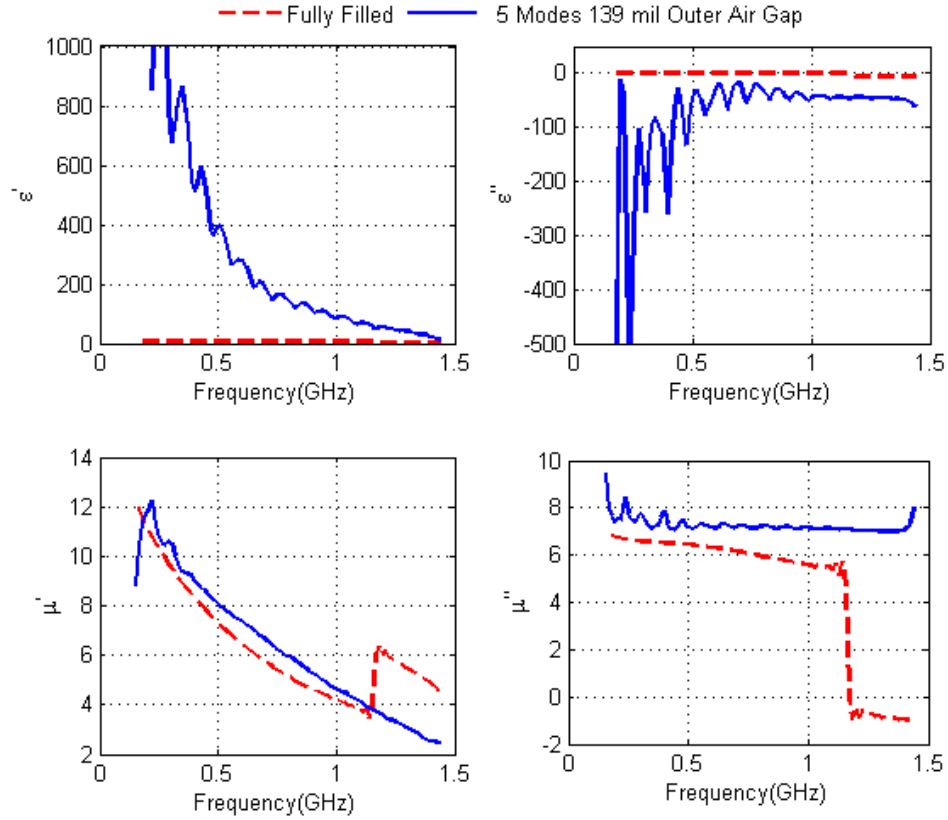


Figure 4.9: Extracted ϵ_r and μ_r extracted from a WaveX sample with a 139 mil outer air gap considering 4 modes using S_{11} and S_{21} . The permeability agrees reasonably with the fully filled solution but the permittivity contains a great deal of error.

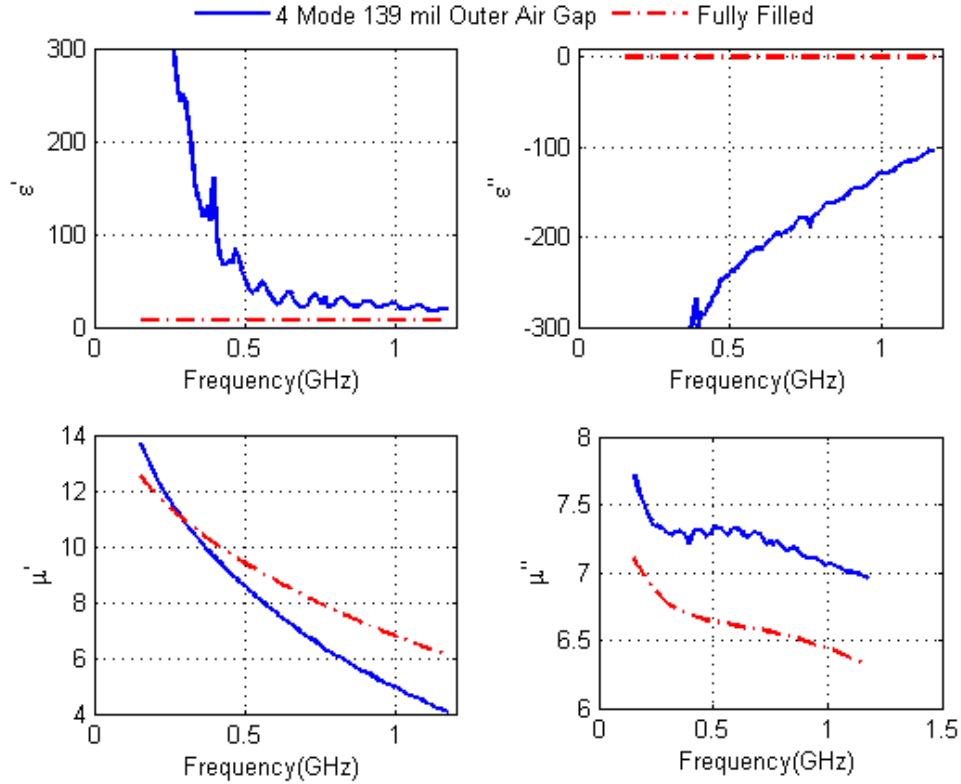


Figure 4.10: Extracted ϵ_r and μ_r extracted from a WaveX sample with a 139 mil outer air gap considering 4 modes. The permeability agrees relatively well with the fully filled solution but the permittivity contains a great deal of error.

One finding discovered during the WaveX testing is the anisotropy of the material. Prior to receiving the GTRI results, a sample was measured in a low frequency stripline to obtain a baseline for comparison to the modal method. The measurements were taken as noted in Section 3.2 and the NRW algorithm was used to extract the values of ϵ_r and μ_r of the material. Due to a high level of noise in the measurements, a windowing function was used to isolate the primary response. The data was transferred to the time domain on the network analyzer where the primary response was located. The window was set at the nulls of the primary response and data transferred back into the frequency domain. This resulted in much cleaner S-parameter measurements, eliminating

a large portion of the noise. As shown in Figure 4.11, the permeability returned a similar trend to the modal method results and GTRI results although shifted lower in magnitude. The values of ϵ'_r settled down to a reasonable value after approximately 500 MHz and then stayed within a reasonable range up to 3 GHz. The values of ϵ''_r oscillated widely across the frequency range which is not readily explained.

As an anisotropic material, WaveX will have different values of permittivity and permeability depending on whether the sample is “in-plane” or “out-of-plane” with the respective electric and magnetic fields. For example, when measuring a sample wrapped around the center conductor of the coaxial line, the “out-of-plane” permittivity and “in-plane” permeability will be extracted. This is because the radially directed electric field travels out of the plane of the material while the azimuthally directed magnetic field is in plane with the material. In the stripline, the material is oriented differently so that the \hat{z} directed electric field is in plane with the sample and the circulating magnetic field is also in plane with the sample. This explains the similarities and differences between the extracted permittivity and permeability values from the stripline and the coax.

A sample of plexiglass was also measured in the stripline using the same method to ensure that accurate results were obtained. The extracted permittivity and permeability values are shown in Figure 4.12. Using a baseline value of $\epsilon_r = 2.6$ and $\mu_r = 1$ the extracted values from the stripline yielded accurate results after approximately 500 MHz.

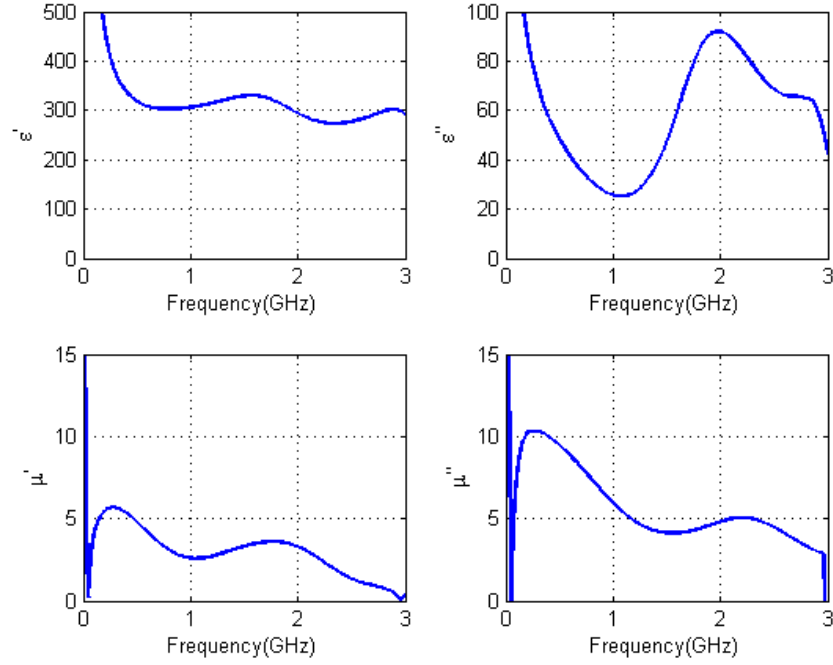


Figure 4.11: The complex permittivity and permeability of WaveX calculated from stripline measurements are shown as $\epsilon_r = \epsilon'_r - j\epsilon''_r$ and $\mu_r = \mu'_r - j\mu''_r$.

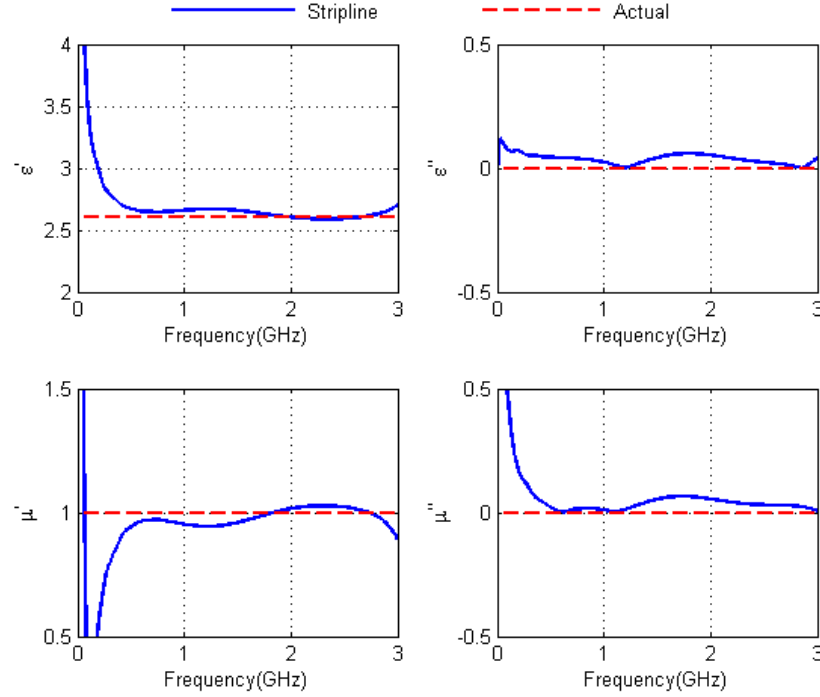


Figure 4.12: Permittivity and permeability of plexiglass calculated from stripline measurements are shown as $\epsilon_r = \epsilon'_r - j\epsilon''_r$ and $\mu_r = \mu'_r - j\mu''_r$.

4.3 Wavenumber Calculation.

The accurate calculation of wavenumbers is critical to the success of the modal method. The wavenumbers are calculated by solving for the roots of (3.7) which is rewritten here as

$$k_{\rho 1n} \varepsilon_2 V_1(k_{\rho 2n} b) W_0(k_{\rho 1n} b) - k_{\rho 2n} \varepsilon_0 V_0(k_{\rho 2n} b) W_1(k_{\rho 1n} b) = 0. \quad (4.2)$$

There are an infinite number of roots to this equation as a result of the oscillatory nature of the Bessel functions which must be found in sequential order.

Given the relatively large outer air gaps considered, the initial approach to solving for the roots of (4.2) was to use a perturbation approach, also known mathematically as a Homotopy method. The method breaks the material thickness into a number of slices which are slowly added to each other until the desired material height is reached. The initial-root guesses used for the first iteration are the roots to the characteristic equation of the unfilled guide. The empty waveguide is then “stepped” out by one thin layer of material and (4.2) is solved using the empty guide solution as the initial guess. This process is repeated using the previous step’s solution as the initial guess for the next iteration. This is done until the final thickness h of the material is reached. The final solutions at that point are the actual values of $\tilde{\gamma}_n$ in the sample region. This assumes that the roots are continuously dependent on the sample thickness.

This method is simple and effective, giving a high likelihood that the numerical technique used to solve (4.2) will converge to the proper root. The major drawback to this lies in the step size (δ) required to ensure that the solution converges to the proper root. This step size is dependent on both the ultimate thickness h and the material

properties of the material under test. A step size of $\delta = h / (15N)$, where N is the total number of modes, was found to sufficiently ensure $\tilde{\gamma}$ convergence to the correct values for materials with low to medium values of ε_r and μ_r [11]. This value of δ works well for the dielectric material but must be increased for higher order modes of the WaveX. Since the total number of iterations is linear with N , the runtime required by this algorithm can quickly become very large. While accurate, this method quickly becomes impractical due to its runtime; therefore, a faster method was needed.

In [8], a Muller root search method was used since the first roots for a highly loaded material are often in close proximity to each other. Muller's method is a variation of the secant method, requiring three initial guesses to the equation. It fits a parabola through these three points and examines the intersection of the parabola with the complex plane. This intersection point becomes the next initial guess and the process is repeated until the root of the function is located. Muller's method works well with complex roots provided the function is analytic. Since Bessel functions of the first kind are analytic everywhere and Bessel functions of the second kind are singular only at the origin, Muller's method is ideally suited for finding the roots of (4.2). The initial guesses for low frequency measurements of low-loss dielectric materials are well estimated by the roots of the characteristic equation for the unfilled coaxial line. Muller's method quickly and accurately locates the roots of the partially filled case which are indeed very close to those of the empty waveguide.

The wavenumber calculations for heavily loaded magnetic materials such as WaveX are much more difficult to solve since the solution is extremely sensitive to the initial guess. In [8], a method using asymptotic expansions of the Bessel functions was

used to determine the initial guesses for use with the Muller root search. Using this approach, the correct wavenumbers were quickly found for a MagRAM filled coaxial line containing a 9 mil inner or outer air gap.

Both the Muller method and the step/perturbation method were implemented to find the roots of (4.2) for the dielectric material. The differences between the two results were found to be on the order of 1×10^{-6} and the runtime of the Muller method was much faster than the Homotopy method. The comparison between the wavenumbers for the empty waveguide and the guide partially filled with dielectric is shown in Table 4.1. Both methods were evaluated to solve for the roots of (4.2) for the WaveX samples. The first mode returned by both methods agreed well, but the perturbation method returned several additional higher order modes not found by the Muller method search. The comparison between the two is shown in Table 4.2.

With the disparity between the results returned by the two methods, the perturbation method was chosen for use in the material parameter extraction. Due to the large air gaps and incredibly complex nature of the media, it is assumed that the Muller method as implemented in [8] does not adequately account for all of the modes present in the region. Additionally, the Muller method did not allow for the consideration of more than 2-3 modes at any time due to the very high attenuation present in $\tilde{\gamma}_n$. This assumption is simple at best and requires greater exploration to confirm.

Table 4.1: Comparison of the wavenumbers in an empty coaxial line and a line partially filled with dielectric with a 123.5 mil outer air gap. The frequency for $\tilde{\gamma}$ is 1 GHz. The Muller and Perturbation method returned nearly identical results.

Empty Coax Line		Perturbation / Muller's Method	
Mode	γ	Mode	$\tilde{\gamma}$
TEM	$0 + 21.0j$	TM ₀₀	$0.07 + 23.4j$
TM ₀₁	771.0	TM ₀₁	$876.2 - 3.7j$
TM ₀₂	1552.1	TM ₀₂	$1606.7 - 2.7j$
TM ₀₃	2331.2	TM ₀₃	$2204.9 + 5.5j$
TM ₀₄	3109.7	TM ₀₄	$3020 + 2.7j$

Table 4.2: Comparison of the wavenumbers returned via the perturbation and Muller methods of a line containing WaveX with a 139 mil outer air gap. The frequency for $\tilde{\gamma}$ is 1 GHz. The material properties used for these calculations are ($\epsilon_r = 83.29 + j49.98$) and ($\mu_r = 4.67 - j7.17$). The difference between the two methods indicate that Muller's Method perhaps misses several modes that are found by the Perturbation method.

	Perturbation Method	Muller's Method
Mode	$\tilde{\gamma}$	$\tilde{\gamma}$
TM ₀₀	$11.4 + 32.1j$	$11.4 + 32.1j$
TM ₀₁	$882.7 + 1.5j$	$2,953.8 + 17.9j$
TM ₀₂	$1,773 + 2.7j$	$9,234.9 + 4.0j$
TM ₀₃	$2,650.5 + 11.9j$	$15,440.4 - 0.1j$
TM ₀₄	$2,953.8 + 17.9j$	$22,252.9 - 4.4j$

V. CONCLUSIONS AND RECOMMENDATIONS FOR FUTURE RESEARCH

The focus of this thesis was the accurate determination of the complex permittivity and permeability of thin samples of materials which partially fill a coaxial transmission line. The primary method used to determine these properties was the modal analysis method developed in [8]. This method takes into account higher order modes excited by air gap discontinuities and should cause the results to converge to the actual material parameters as increasing numbers of modes are considered. This assumes that the axially symmetric higher order modes are the only significant source of error in the measured values. Other methods such as perturbation techniques and a low frequency stripline were briefly investigated as well for comparison purposes.

Both a low loss dielectric material and high loss magnetic material were investigated in this thesis. The dielectric was used to prove the effectiveness of the modal method with large air gaps. The intent was to utilize a 2D complex root search using two independently obtained values of S_{21} to solve for ϵ_r and μ_r since it was unknown whether the S_{11} magnitudes would be large to return accurate results due to the large air gap. It turns out that that the S_{11} values for the dielectric, although very small, were good enough to be used in the 2D root search to solve for ϵ_r and μ_r . This technique was then extended to measured samples of a 20 mil thick sample of the magnetic material WaveX. The WaveX material lacks well quantified permittivity and permeability data, so the low frequency stripline method was briefly explored to provide data to compare to the modal method. The development of this technique is shown in Chapter 3 along with

the modal analysis method development. The results of both methods are reported in Chapter 4.

5.1 Future Research

There are several avenues that could be explored to further the research contained within this thesis.

5.1.1. Air Gap Sensitivity Analysis. This research considered both dielectric and magnetic materials containing outer air gaps that accounted for over 75% and 87% respectively of the cross section of the line. The modal method performed well for the dielectric sample considering such a large air gap, but performed very poorly for the WaveX material. The performance of the dielectric sample was expected based upon results of previous research by Fehlen. The MagRAM samples considered in [8] contained only a 9 mil outer air gap representing only approximately 1.5% of the cross section of the line. The method performed well for this scenario, but still contained some error, especially at the lower frequencies. It is not surprising then, given the very large air gap considered in this research, that the method would perform poorly for the WaveX samples.

One avenue of future exploration could be the sensitivity of the modal method to the size of the air gap for lossy magnetic materials. The use of a more well quantified material is recommended as one of the challenges associated with WaveX was the availability of independently determined values of ϵ_r and μ_r .

5.1.2. Consideration for Anisotropic Material. The modal method development performed in this thesis assumes that the MUT is simple media (i.e. linear, homogenous, and isotropic). As it turns out, the WaveX samples are highly anisotropic; therefore, some of the assumptions made in the field developments could be invalidated. A closer examination of the effects on the field developments for an anisotropic material would be beneficial beginning with Maxwell's equations.

APPENDIX A: MAXWELL'S EQUATIONS

The comprehension of electromagnetic wave theory and the mode-matching technique begins with the understanding of Maxwell's equations which are summarized here based on the developments from [2, 6, 10]. This understanding is the basis upon which all field developments for waveguides are built.

$$\nabla \times \vec{E} = -\vec{M} - j\omega\vec{B} \quad (\text{A-1})$$

$$\nabla \times \vec{H} = \vec{J} + j\omega\vec{D} \quad (\text{A-2})$$

$$\nabla \cdot \vec{D} = q_{ev} \quad (\text{A-3})$$

$$\nabla \cdot \vec{B} = q_{mv} \quad (\text{A-4})$$

The two curl equations known respectively as Faraday's Law and Ampere's Law relate the electric (\vec{E}) and magnetic (\vec{H}) field intensities to the corresponding magnetic current and flux densities (\vec{M} , \vec{B}) or electric current and flux densities (\vec{J} , \vec{D}) as a function of angular frequency. The two divergence equations known as Gauss's Law for Electric and Magnetic fields relate the electric or magnetic flux densities to the electric or magnetic charge densities. This research assumes that all materials of interest are linear, homogeneous, and isotropic; therefore,

$$\vec{D} = \epsilon\vec{E} \quad (\text{A-5})$$

$$\vec{B} = \mu\vec{H} \quad (\text{A-6})$$

with ϵ and μ being the permittivity and permeability of the material. Making this substitution into Maxwell's Equations presents them in their simplified form as

$$\nabla \times \vec{E} = -\vec{M} - j\omega\mu\vec{H} \quad (\text{A-7})$$

$$\nabla \times \vec{H} = \vec{J} + j\omega\varepsilon\vec{E} \quad (\text{A-8})$$

$$\nabla \cdot \vec{E} = \frac{q_{ev}}{\varepsilon} \quad (\text{A-9})$$

$$\nabla \cdot \vec{H} = \frac{q_{mv}}{\mu}. \quad (\text{A-10})$$

Maxwell's equations, (A-7) through (A-10) are first-order, coupled, partial differential equations. They cannot be solved directly to obtain the electric and magnetic fields; however, they can be used to form second-order, uncoupled, partial differential equations which are readily solvable for the fields in the system.

APPENDIX B: HELMHOLTZ WAVE EQUATIONS & VECTOR POTENTIALS

The Helmholtz wave equation for the electric fields is formed by taking the curl of both sides of Faraday's Law (A-7)

$$\nabla \times \nabla \times \vec{E} = -\nabla \times \vec{M} - j\omega\mu\nabla \times \vec{H}. \quad (\text{B-1})$$

Using the vector identity

$$\nabla \times \nabla \times \vec{A} = \nabla(\nabla \cdot \vec{A}) - \nabla^2 \vec{A}, \quad (\text{B-2})$$

and Ampere's Law (A-8), equation (B-1) now becomes

$$\nabla(\nabla \cdot \vec{E}) - \nabla^2 \vec{E} = -\nabla \times \vec{M} - j\omega\mu(\vec{J} + j\omega\varepsilon\vec{E}). \quad (\text{B-3})$$

Applying Gauss's Law (A-9) and simplifying, Helmholtz's electric field wave equation becomes

$$\nabla^2 \vec{E} + k^2 \vec{E} = \nabla \times \vec{M} + j\omega\mu\vec{J} + \frac{1}{\varepsilon} q_{ev} \quad (\text{B-4})$$

where

$$k^2 = \omega^2 \varepsilon \mu. \quad (\text{B-5})$$

Ampere's Law can be treated in the same manner yielding Helmholtz's magnetic field wave equation

$$\nabla^2 \vec{H} + k^2 \vec{H} = -\nabla \times \vec{J} + j\omega\varepsilon\vec{M} + \frac{1}{\mu} q_{mv}. \quad (\text{B-6})$$

Assuming no electric or magnetic sources are present in the region, (B-4) and (B-6) reduce to the source-free electric and magnetic field Helmholtz wave equations:

$$\nabla^2 \vec{E} + k^2 \vec{E} = 0 \quad (\text{B-7})$$

$$\nabla^2 \bar{H} + k^2 \bar{H} = 0. \quad (\text{B-8})$$

The fields can now be solved for using vector potentials and the separation of variables technique described in [2]. The wave equation of the form of (B-7) or (B-8) can be expressed in terms of cylindrical coordinates for a coaxial system:

$$\nabla^2 \psi(\rho, \phi, z) + k^2 \psi(\rho, \phi, z) = 0. \quad (\text{B-9})$$

When expanding (B-9) in cylindrical coordinates, the wave equation becomes

$$\frac{1}{\rho} \frac{\partial}{\partial \rho} \left(\rho \frac{\partial \psi}{\partial \rho} \right) + \frac{1}{\rho^2} \frac{\partial^2 \psi}{\partial \phi^2} + \frac{\partial^2 \psi}{\partial z^2} + k^2 \psi = 0 \quad (\text{B-10})$$

where ψ is a scalar function that can represent a field or vector potential. Assuming that $\psi(\rho, \phi, z)$ has a separable solution of the form

$$\psi(\rho, \phi, z) = f(\rho) g(\phi) h(z), \quad (\text{B-11})$$

equation (B-10) can be rewritten as

$$\frac{1}{f} \frac{d^2 f}{d\rho^2} + \frac{1}{f} \frac{1}{\rho} \frac{df}{d\rho} + \frac{1}{g} \frac{1}{\rho^2} \frac{d^2 g}{d\phi^2} + \frac{1}{h} \frac{d^2 h}{dz^2} = -k^2. \quad (\text{B-12})$$

Since the next to last and last term on the left side of (B-12) are functions of a single variable, they must be constants and are determined to be

$$\frac{1}{g} \frac{d^2 g}{d\phi^2} = -m^2 \quad (\text{B-13})$$

$$\frac{1}{h} \frac{d^2 h}{dz^2} = -k_z^2. \quad (\text{B-14})$$

Substituting these results into (B-12) yields the reduced equation

$$\frac{\rho^2}{f} \frac{d^2 f}{d\rho^2} + \frac{\rho}{f} \frac{df}{d\rho} + (-m^2) + \rho^2 (k^2 - k_z^2) = 0. \quad (\text{B-15})$$

Rearranging the terms of (B-15) and defining

$$k_\rho^2 = k^2 - k_z^2 \quad (\text{B-16})$$

results in the following equations defining f, g, and h respectively:

$$\rho^2 \frac{d^2 f}{d\rho^2} + \rho \frac{df}{d\rho} + \left[(k_\rho \rho)^2 - m^2 \right] f = 0. \quad (\text{B-17})$$

$$\frac{d^2 g}{d\phi^2} = -m^2 g \quad (\text{B-18})$$

$$\frac{d^2 h}{dz^2} = -k_z^2 h \quad (\text{B-19})$$

Equation (B-17) is readily identified as the Bessel differential equation which means the general solution will be a linear combination of Bessel or Hankel functions.

For the coaxial line in this research, the field will be a standing wave in the $\hat{\rho}$ direction yielding the solution

$$f(\rho) = AJ_m(k_\rho \rho) + BY_m(k_\rho \rho) \quad (\text{B-20})$$

where J_m and Y_m represent Bessel functions of the first and second kind respectively of order m.

The solutions to (B-18) and (B-19) are well documented. For the case of the \hat{z} directed coaxial waveguide, the solutions to these are

$$g(\phi) = C \cos(m\phi) + D \sin(m\phi) \quad (\text{B-21})$$

$$h(z) = Ee^{-\gamma z} + Fe^{\gamma z} \quad (\text{B-22})$$

where

$$\gamma = jk_z. \quad (\text{B-23})$$

The solution to the Helmholtz wave equation (B-9) can now be expressed by a product of the individual solutions of (B-20), (B-21), and (B-22)

$$\psi_{m,n}(\rho, \phi, z) = \left[A_{m,n} J_m(k_\rho \rho) + B_{m,n} Y_m(k_\rho \rho) \right] \left[C_{m,n} \cos(m\phi) + D_{m,n} \sin(m\phi) \right] \times \left[E_{m,n} e^{-\gamma z} + F_{m,n} e^{\gamma z} \right] \quad (\text{B-24})$$

where subscripts m and n are added for denoting unique solutions and

$$k_{\rho n} = \sqrt{\gamma_n^2 - k^2} \quad (\text{B-25})$$

APPENDIX C: FIELDS IN A COAXIAL WAVEGUIDE

C.1 TM fields in a Coaxial Guide

For a linear, isotropic, homogenous material, the electric and magnetic vector potentials (F and A respectively) are

$$\begin{aligned}\vec{F} &= 0 \\ \vec{A} &= \hat{z}A_z.\end{aligned}\tag{C.1}$$

The magnetic potential \vec{A} takes the form of the potential function (B-24) and becomes

$$A_z = \left[A_{m,n}J_m(k_\rho\rho) + B_{m,n}Y_m(k_\rho\rho) \right] \left[C_{m,n}\cos(m\phi) + D_{m,n}\sin(m\phi) \right] \times \left[E_{m,n}e^{-\gamma z} + F_{m,n}e^{\gamma z} \right]\tag{C-2}$$

The potentials from (C.1) are then substituted into the following field relationships:

$$\begin{aligned}\vec{E} &= \frac{1}{j\omega\epsilon\mu} \left[k^2\vec{A} + \nabla(\nabla \cdot \vec{A}) \right] - \frac{\nabla \times \vec{F}}{\epsilon} \\ \vec{H} &= \frac{\nabla \times \vec{A}}{\mu} + \frac{1}{j\omega\epsilon\mu} \left[k^2\vec{F} + \nabla(\nabla \cdot \vec{F}) \right].\end{aligned}\tag{C-3}$$

Solving (C-3) using the magnetic vector potential from (C-2) yields the generating functions for the TM^z fields present in the coaxial waveguide:

$$\begin{aligned}E_\rho &= \frac{1}{j\omega\epsilon\mu} \frac{\partial^2 A_z}{\partial \rho \partial z} & H_\rho &= \frac{1}{\mu} \frac{1}{\rho} \frac{\partial A_z}{\partial \phi} \\ E_\phi &= \frac{1}{j\omega\epsilon\mu} \frac{1}{\rho} \frac{\partial^2 A_z}{\partial \rho \partial z} & H_\phi &= -\frac{1}{\mu} \frac{\partial A_z}{\partial \rho} \\ E_z &= \frac{1}{j\omega\epsilon\mu} \left(\frac{\partial^2}{\partial z^2} + k^2 \right) A_z & H_z &= 0\end{aligned}$$

Filling in the magnetic vector potential into these generating functions yields the TM^z field components in the guide:

$$\begin{aligned}
E_\rho &= \frac{-k_\rho \gamma}{j\omega\epsilon\mu} \left[AJ'_m(k_\rho \rho) + BY'_m(k_\rho \rho) \right] \left[C \cos(m\phi) + D \sin(m\phi) \right] \left[Ee^{-\gamma z} - Fe^{\gamma z} \right] \\
E_\phi &= \frac{-m\gamma}{j\omega\epsilon\mu\rho} \left[AJ_m(k_\rho \rho) + BY_m(k_\rho \rho) \right] \left[C \sin(m\phi) - D \cos(m\phi) \right] \left[Ee^{-\gamma z} - Fe^{\gamma z} \right] \\
E_z &= \frac{k_\rho^2}{j\omega\epsilon\mu} \left[AJ_m(k_\rho \rho) + BY_m(k_\rho \rho) \right] \left[C \cos(m\phi) + D \sin(m\phi) \right] \left[Ee^{-\gamma z} + Fe^{\gamma z} \right] \\
H_\rho &= \frac{m}{\mu\rho} \left[AJ_m(k_\rho \rho) + BY_m(k_\rho \rho) \right] \left[C \sin(m\phi) - D \cos(m\phi) \right] \left[Ee^{-\gamma z} + Fe^{\gamma z} \right] \\
H_\phi &= \frac{-k_\rho}{\mu} \left[AJ'_m(k_\rho \rho) + BY'_m(k_\rho \rho) \right] \left[C \cos(m\phi) + D \sin(m\phi) \right] \left[Ee^{-\gamma z} + Fe^{\gamma z} \right]
\end{aligned}$$

After the field components are known, boundary conditions at both the inner ($\rho=a$) and outer ($\rho=c$) walls of the waveguide must be applied. For this scenario, both walls are considered to be PEC; therefore, this requires that the tangential electric fields at both walls must be zero.

$$\begin{aligned}
E_{\phi,z}(\rho, \phi, z)|_{\rho=a} &= 0 \Rightarrow AJ_m(k_\rho a) + BY_m(k_\rho a) = 0 \\
E_{\phi,z}(\rho, \phi, z)|_{\rho=c} &= 0 \Rightarrow AJ_m(k_\rho c) + BY_m(k_\rho c) = 0
\end{aligned}$$

Solving for the constant A at the

$$A = -B \frac{Y_m(k_\rho a)}{J_m(k_\rho a)} \quad \text{inner wall yields}$$

This is then substituted into the field equations producing

$$\begin{aligned}
E_\rho &= \frac{-k_{\rho n} \gamma_n B_{mn}}{j\omega\epsilon\mu J_m(k_{\rho n} a)} V_1(k_{\rho n} \rho) \left[C \cos(m\phi) + D \sin(m\phi) \right] \left[Ee^{-\gamma_n z} - Fe^{\gamma_n z} \right] \\
E_\phi &= \frac{-m\gamma_n B_{mn}}{j\omega\epsilon\mu J_m(k_{\rho n} a)} \left(\frac{1}{\rho} \right) V_0(k_{\rho n} \rho) \left[C \sin(m\phi) - D \cos(m\phi) \right] \left[Ee^{-\gamma_n z} - Fe^{\gamma_n z} \right] \\
E_z &= \frac{k_{\rho n}^2 B_{mn}}{j\omega\epsilon\mu J_m(k_{\rho n} a)} V_0(k_{\rho n} \rho) \left[C \cos(m\phi) + D \sin(m\phi) \right] \left[Ee^{-\gamma_n z} + Fe^{\gamma_n z} \right]
\end{aligned}$$

$$H_\rho = \frac{mB_{mn}}{\mu J_m(k_{\rho n}a)} \left(\frac{1}{\rho} \right) V_0(k_{\rho n}\rho) [C \sin(m\phi) - D \cos(m\phi)] [Ee^{-\gamma_n z} + Fe^{\gamma_n z}]$$

$$H_\phi = \frac{-k_{\rho n}B_{mn}}{\mu J_m(k_{\rho n}a)} V_1(k_{\rho n}\rho) [C \cos(m\phi) + D \sin(m\phi)] [Ee^{-\gamma_n z} + Fe^{\gamma_n z}],$$

where

$$V_m(k_{\rho}\rho) = [J_m(\alpha\rho)Y_0(\alpha a) - J_0(\alpha a)Y_m(\alpha\rho)].$$

Assuming the waveguide is axially symmetric (m=0) and only accounting for the forward propagating fields, the field components reduce to

$$E_\rho = \frac{-k_{\rho n}\gamma_n B_{0,n}}{j\omega\epsilon\mu J_0(k_{\rho n}a)} V_1(k_{\rho n}\rho) e^{-\gamma_n z}$$

$$E_z = \frac{k_{\rho n}^2 B_{0,n}}{j\omega\epsilon\mu J_0(k_{\rho n}a)} V_0(k_{\rho n}\rho) e^{-\gamma_n z}$$

$$H_\phi = \frac{-k_{\rho n}B_{0,n}}{\mu J_0(k_{\rho n}a)} V_1(k_{\rho n}\rho) e^{-\gamma_n z}$$

with the E_ϕ and H_ρ fields going to zero due to axial symmetry. The characteristic equation needed to solve for γ_n is produced by applying the boundary conditions at the outer wall and yields

$$[J_0(k_{\rho n}c)Y_0(k_{\rho n}a) - J_0(k_{\rho n}a)Y_0(k_{\rho n}c)] = 0 \quad (3.4)$$

where $k_{\rho n} = \sqrt{k^2 + \gamma_n^2}$. For the TEM mode, $\gamma_n = k$ and from [13], the value for γ_n for

TM_{0n} modes is well estimated by

$$\gamma_n = \sqrt{\left(\frac{n\pi}{(c-a)}\right)^2 - k^2}$$

where c and a represent the outer and inner radii of the waveguide [13]. This is used as the initial guess when numerically solving (3.4) for the actual value of γ_n for higher order axially symmetric TM modes.

C.2 TEM Fields in a Coaxial Guide

The dominant field present in a fully filled coaxial waveguide is the TEM^Z field. This field is also sometimes referred to as the TM_{00} mode and can be developed from the axially symmetric ($m=0$) TM^Z fields which were previously derived. These axially symmetric modes allow for the possibility of $k_\rho = 0$ which is found by examining the $E_z(\rho = a, b) = 0$ boundary condition. This is referred to as the $n=0$ mode. In this case, $k_z = k$ since $k_\rho = 0$.

The TEM fields are developed by taking the limit as $k_\rho \rightarrow 0$ of the TM fields developed above. The small argument approximations and logarithmic identity shown in Table C.1 are applied to yield the resulting TEM fields.

Table C.1: Small Argument and Logarithm Identities

$\lim_{x \rightarrow 0} J_0(x) \sim 1$	$\lim_{x \rightarrow 0} Y_1(x) \sim \frac{-2}{\pi x}$
$\lim_{x \rightarrow 0} J_1(x) \sim \frac{x}{2}$	$\lim_{x \rightarrow 0} x^\alpha \ln(x) \sim 0$
$\lim_{x \rightarrow 0} Y_0(x) \sim \frac{2}{\pi} \ln\left(\frac{\tilde{\gamma}x}{2}\right)$	$(\alpha = \text{constant}, \text{Re}\{\alpha\} > 0)$

$$\begin{aligned}
\lim_{k_{\rho n} \rightarrow 0} E_{\rho} &= \frac{k_{\rho n} \gamma_n B_{0,n}}{j\omega \varepsilon \mu} \left[\left(\frac{k_{\rho n} \rho}{2} \right) \left(\frac{2}{\pi} \ln \left(\frac{\gamma k_{\rho n} a}{2} \right) \right) - (1) \left(\frac{-2}{\pi k_{\rho n} \rho} \right) \right] e^{-\gamma_n z} \\
&= \frac{\gamma_n B_{0,n}}{j\omega \varepsilon \mu} \left[\left(\frac{2k_{\rho n} \rho}{\pi a \gamma} \right) \left(\frac{\gamma k_{\rho n} a}{2} \ln \left(\frac{k_{\rho n} a}{2} \right) \right) + \frac{2}{\pi \rho} \right] e^{-\gamma_n z} \\
&= \frac{2k B_{0,n}}{\pi \omega \varepsilon \mu} \left[\frac{1}{\rho} \right] e^{-jkz} \quad \dots \quad \lim_{k_{\rho n} \rightarrow 0} k^2 = k_{\rho n}^2 + k_z^2 = \omega^2 \varepsilon \mu
\end{aligned}$$

$$\begin{aligned}
\lim_{k_{\rho n} \rightarrow 0} E_z &= \frac{k_{\rho n}^2 B_{0,n}}{j\omega \varepsilon \mu} \left[(1) \left(\frac{2}{\pi} \ln \left(\frac{\gamma k_{\rho n} a}{2} \right) \right) - (1) \left(\frac{2}{\pi} \ln \left(\frac{\gamma k_{\rho n} \rho}{2} \right) \right) \right] e^{-\gamma_n z} \\
&= \frac{k_{\rho n} B_{0,n}}{j\omega \varepsilon \mu} \left[\frac{4\gamma k_{\rho n} a}{2\pi a \gamma} \ln \left(\frac{\gamma k_{\rho n} a}{2} \right) - \frac{4\gamma k_{\rho n} \rho}{2\pi \rho \gamma} \ln \left(\frac{\gamma k_{\rho n} \rho}{2} \right) \right] e^{-\gamma_n z} \\
&= 0
\end{aligned}$$

$$\begin{aligned}
\lim_{k_{\rho n} \rightarrow 0} H_{\phi} &= \frac{k_{\rho n} B_{0,n}}{\mu} \left[\left(\frac{k_{\rho n} \rho}{2} \right) \left(\frac{2}{\pi} \ln \left(\frac{\gamma k_{\rho n} a}{2} \right) \right) - (1) \left(\frac{-2}{\pi k_{\rho n} \rho} \right) \right] e^{-\gamma_n z} \\
&= \frac{B_{0,n}}{\mu} \left[\left(\frac{2k_{\rho n} \rho}{\pi a \gamma} \right) \left(\frac{\gamma k_{\rho n} a}{2} \ln \left(\frac{\gamma k_{\rho n} a}{2} \right) \right) + \frac{2}{\pi \rho} \right] e^{-\gamma_n z} \\
&= \frac{2B_{0,n}}{\pi \mu} \left[\frac{1}{\rho} \right] e^{-\gamma_n z} \\
&= \left(\frac{k_z \omega \varepsilon \mu}{k_z \omega \varepsilon \mu} \right) \frac{2B_{0,n}}{\pi \mu} \left[\frac{1}{\rho} \right] e^{-\gamma_n z} \\
&= \left(\frac{2k B_{0,n}}{\pi \omega \varepsilon \mu} \right) \frac{\omega \varepsilon \mu}{\omega \mu \sqrt{\varepsilon \mu}} \left[\frac{1}{\rho} \right] e^{-\gamma_n z} \quad \dots \quad \lim_{k_{\rho n} \rightarrow 0} k^2 = k_{\rho n}^2 + k_z^2 = \omega^2 \varepsilon \mu \\
&= \left(\frac{2k B_{0,n}}{\pi \omega \varepsilon \mu} \right) \frac{1}{Z_{TEM}} \left[\frac{1}{\rho} \right] e^{-\gamma_n z} \quad \dots \quad Z_{TEM} = \sqrt{\frac{\mu}{\varepsilon}}
\end{aligned}$$

Summarily, axially symmetric TM^Z fields in a coaxial waveguide reduce to the dominant TEM fields

$$\begin{aligned} E_\rho &= \Upsilon \left[\frac{1}{\rho} \right] e^{-jkz} \\ H_\phi &= \frac{\Upsilon}{Z_{TEM}} \left[\frac{1}{\rho} \right] e^{-jkz} \end{aligned} \tag{C.5}$$

where

$$\Upsilon = \frac{2kB_{0,n}}{\pi\omega\epsilon\mu} \tag{C.6}$$

APPENDIX D: GTRI WAVEX RESULTS

Multiple samples of WaveX (WX-A020) were measured by researchers at GTRI. The low frequency measurements were taken using an impedance analyzer fixture while the high frequency measurements were taken using a focused beam system. Both the in-plane and out-of-plane complex permittivity was extracted along with the in-plane complex permeability. The “Old” samples correspond to a WaveX sample manufactured in the 2007 timeline while the “New” samples correspond to a WaveX sample manufactured sometime in 2011. The presumption is that manufacturing processes have improved between the two samples explaining the differences. The extracted parameters are displayed in Figures D.1 – D.3.

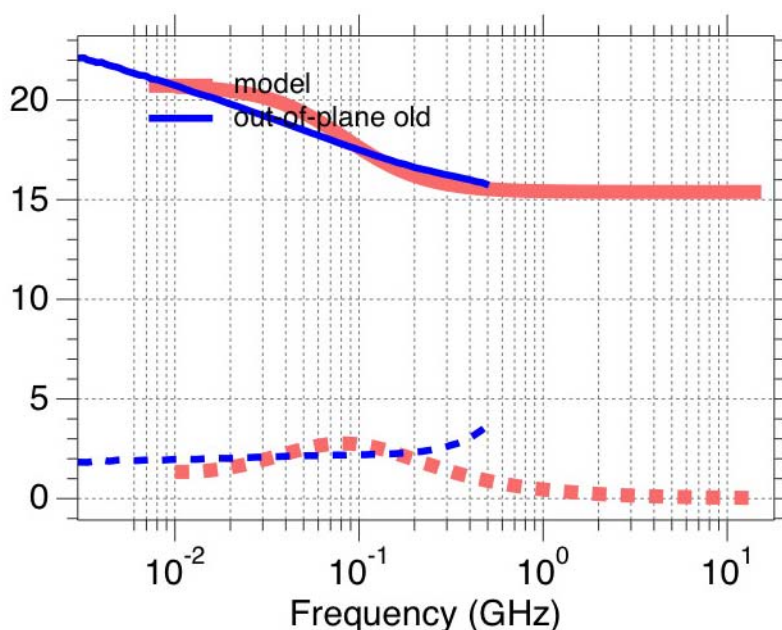


Figure D.1: Extracted out-of-plane permittivity of “Old” WaveX sample

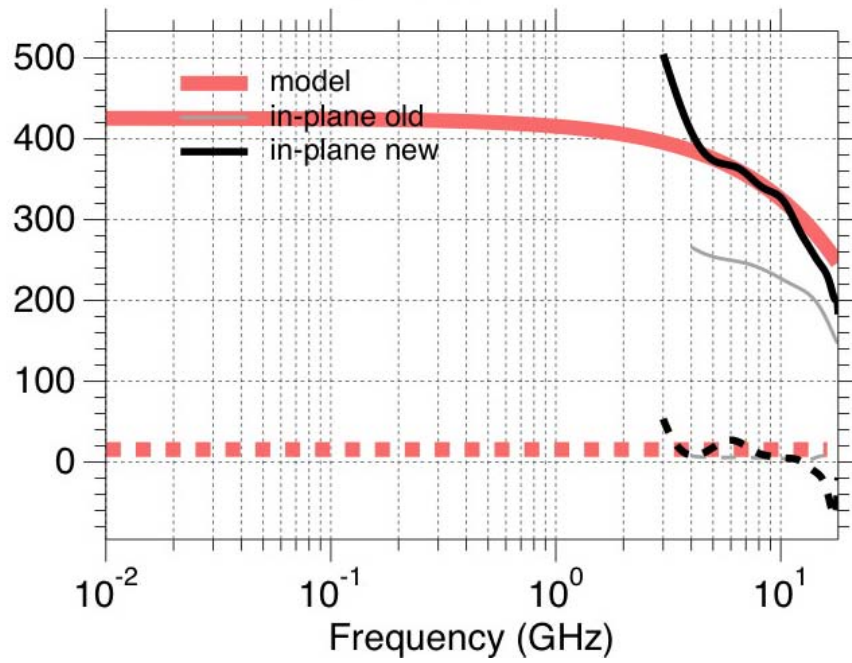


Figure D.2: Extracted in-plane permittivity of “Old” and “New” WaveX samples

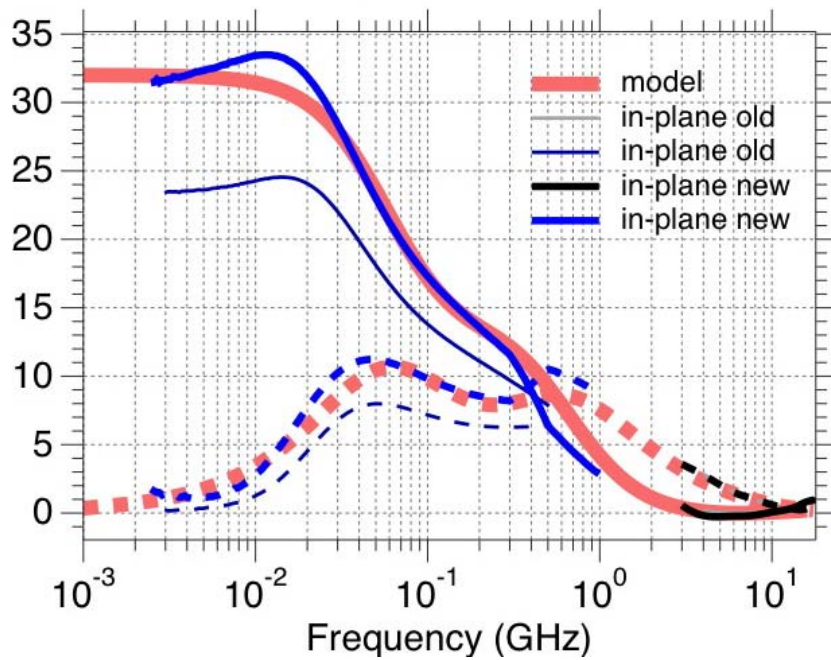


Figure D.3: Extracted in-plane permeability of “Old” and “New” WaveX samples

BIBLIOGRAPHY

- [1] Baker-Jarvis, J.R., M.D. Janezic, J.H. Grosvenor Jr., and R.G. Geyer. *Transmission/Reflection and Short-Circuit Line Methods for Measuring Permittivity and Permeability (Tech. Note 1355-R)*. Nat. Inst. Stands. Tech., Dec 1993.
- [2] Balanis, Constantine A., *Advanced Engineering Electromagnetics*, John Wiley & Sons, 1st edition, 1989.
- [3] Burden, R.L. and J.D. Faires, *Numerical Analysis Theory and Applications*, Brooks Cole, 9th edition, 2010.
- [4] Champlin, K.S. and G.H. Glover, "Gap Effect in Measurement of Large Permittivities," *IEEE Transactions on Microwave Theory and Techniques*, vol. 14, no. 8, pp 397-398, 1966.
- [5] Chen, L.F., C.K. Ong, C.P. Neo, V.V. Varadan, and V.K. Varadan, *Microwave Electronics Measurement and Materials Characterization*, John Wiley & Sons, 1st edition, 2004.
- [6] Collin, Robert E. *Field Theory of Guided Waves*. IEEE Press, New Jersey, 2nd edition, 1990.
- [7] Engen, G.F. and C. Hoer, "Thru-Reflect-Line: An Improved Technique for Calibrating the Dual Six-Port Automatic Network Analyzer," *IEEE Transactions on Microwave Theory and Techniques*, vol. 27, no. 12, pp. 987-993, 1979.
- [8] Fehlen, Ronald G., *Air Gap Error Compensation for Coaxial Transmission Line Method of Electromagnetic Material Characterization*, Master's thesis, School of Engineering and Management, Air Force Institute of Technology (AU), Wright-Patterson AFB OH, Mar 2006
- [9] Gardiol, Fred E., "Higher-Order Modes in Dielectrically Loaded Rectangular Waveguides," *IEEE Transactions on Microwave Theory and Techniques*, vol. 16, no. 11, pp. 919-924, 1968.
- [10] Harrington, Roger F., *Time-Harmonic Electromagnetic Fields*, McGraw-Hill, Inc., 1961
- [11] Hyde, Milo W. IV, M.J. Havrilla, and E.J. Rothwell, "A Transmission-Based Material-Characterization Technique Using a Partially-Filled Rectangular Waveguide," unpublished

- [12] Levenberg, Kenneth, "A Method for the Solution of Certain Non-Linear Problems in Least Squares," *The Quarterly of Applied Mathematics*, 2(2), pp. 164-168, 1944.
- [13] Marcuvitz, N. "Waveguide Handbook", MIT Radiation Laboratory Series, 10, 1951
- [14] Marquardt, Donald, "An Algorithm for Least-Squares Estimation of Nonlinear Parameters," *SIAM Journal on Applied Mathematics*, 11(2), pp. 431-441, 1963.
- [15] Nicolson A. M. and G. F. Ross. "Measurement of the Intrinsic Properties of Materials by Time-Domain Techniques." *IEEE Transaction on Instrumentation and Measurement*, vol. 19, no. 4, pp. 377-382, 1970.
- [16] Weir, W.B., "Automatic Measurement of Complex Dielectric Constant and Permeability at Microwave Frequencies." *Proceedings of the IEEE*, vol. 62, no. 1, pp. 33-36, 1974.
- [17] Wexler, Alvin, "Solution of Waveguide Discontinuities by Modal Analysis," *IEEE Transactions on Microwave Theory and Techniques*, vol. 15, no. 9, pp. 508-517, 1967.
- [18] Wilson, Scott B., "Modal analysis of the 'gap effect' in waveguide dielectric measurements," *IEEE Transactions on Microwave Theory and Techniques*, vol. 36, no. 4, pp. 752-756, 1988.

REPORT DOCUMENTATION PAGE				Form Approved OMB No. 074-0188	
<p>The public reporting burden for this collection of information is estimated to average 1 hour per response, including the time for reviewing instructions, searching existing data sources, gathering and maintaining the data needed, and completing and reviewing the collection of information. Send comments regarding this burden estimate or any other aspect of the collection of information, including suggestions for reducing this burden to Department of Defense, Washington Headquarters Services, Directorate for Information Operations and Reports (0704-0188), 1215 Jefferson Davis Highway, Suite 1204, Arlington, VA 22202-4302. Respondents should be aware that notwithstanding any other provision of law, no person shall be subject to a penalty for failing to comply with a collection of information if it does not display a currently valid OMB control number.</p> <p>PLEASE DO NOT RETURN YOUR FORM TO THE ABOVE ADDRESS.</p>					
1. REPORT DATE (DD-MM-YYYY) 22-03-2012		2. REPORT TYPE Master's Thesis		3. DATES COVERED (From – To) Sep 2010 – Mar 2012	
4. TITLE AND SUBTITLE Low Frequency Material Characterization of Thin Substrates in a Coaxial Transmission Line				5a. CONTRACT NUMBER	
				5b. GRANT NUMBER	
				5c. PROGRAM ELEMENT NUMBER	
6. AUTHOR(S) Cole, Lee B. , Captain, USAF				5d. PROJECT NUMBER	
				5e. TASK NUMBER	
				5f. WORK UNIT NUMBER	
7. PERFORMING ORGANIZATION NAMES(S) AND ADDRESS(S) Air Force Institute of Technology Graduate School of Engineering and Management (AFIT/EN) 2950 Hobson Way WPAFB OH 45433-7765				8. PERFORMING ORGANIZATION REPORT NUMBER AFIT/GE/ENG/12-10	
9. SPONSORING/MONITORING AGENCY NAME(S) AND ADDRESS(ES) Air Force Research Laboratory, Sensors Directorate Attn: Mr. Garrett Stenholm 2591 K Street, Bldg. 254 Wright-Patterson AFB, OH 45433-7602 (937) 244-9179 ; garrett.stenholm@wpafb.af.mil				10. SPONSOR/MONITOR'S ACRONYM(S) AFRL/RYS	
				11. SPONSOR/MONITOR'S REPORT NUMBER(S)	
12. DISTRIBUTION/AVAILABILITY STATEMENT DISTRIBUTION A. APPROVED FOR PUBLIC RELEASE; DISTRIBUTION UNLIMITED					
13. SUPPLEMENTARY NOTES This material is declared a work of the U.S. Government and is not subject to copyright protection in the United States.					
14. ABSTRACT This research analyzes the complex permittivity and permeability of thin material samples at low frequencies in the presence of large outer air gaps. It uses the modal method developed in previous research to account for the errors introduced to the system by the presence of higher order modes excited by the air gaps. The theoretical scattering parameters returned by the modal method are compared to the measured scattering parameters and the difference between the two is minimized using a complex root search algorithm. The method is tested with samples of a dielectric material and the magnetic material WaveX which respectively fill 22% and 12.5% of the distance between the inner and outer conductors. The method accurately determined the complex permittivity of the dielectric samples, appearing to converge after the inclusion of 10 higher order modes. The method performed poorly for the WaveX material, particularly for complex permittivity. Assumptions of an axially symmetric field environment in the sample region and a linear, isotropic, homogeneous material were made. Upon evaluation, the axially symmetric environment is likely disrupted due to discontinuities arising from the material wrapping around the inner conductor. The material also exhibited strong anisotropic tendencies upon further evaluation.					
15. SUBJECT TERMS Electromagnetic properties, Electromagnetic interference, Electromagnetic compatibility, Waveguide discontinuities, Material characterization measurements, Modal Field Analysis, Partially filled waveguide					
16. SECURITY CLASSIFICATION OF:			17. LIMITATION OF ABSTRACT UU	18. NUMBER OF PAGES 95	19a. NAME OF RESPONSIBLE PERSON Dr. Michael J. Havrilla (ENG)
REPORT U	ABSTRACT U	c. THIS PAGE U			19b. TELEPHONE NUMBER (Include area code) (937) 255-3636 x4582 michael.havrilla@afit.edu

Standard Form 298 (Rev. 8-98)

Prescribed by ANSI Std. Z39-18